PAPER • OPEN ACCESS

Theory and modeling of electron fishbones

To cite this article: G Vlad *et al* 2016 *New J. Phys.* **18** 105004

View the article online for updates and enhancements.

Related content

- Electron fishbone simulations in tokamak equilibria using XHMGC
  G. Vlad, S. Briguglio, G. Fogaccia et al.

- Saturation of single toroidal number Alfvén modes
  X Wang and S Briguglio

- Single-n versus multiple-n simulations of Alfvénic modes
  G. Vlad, S. Briguglio, G. Fogaccia et al.

Recent citations

- Transport theory of phase space zonal structures
  Matteo Valerio Falessi and Fulvio Zonca

- Nonlinear dynamics of shear Alfvén fluctuations in divertor tokamak test facility plasmas
  T. Wang *et al*

- Shear Alfvén fluctuation spectrum in divertor tokamak test facility plasmas
  T. Wang *et al*

IOP ebooks™

Bringing you innovative digital publishing with leading voices to create your essential collection of books in STEM research.

Start exploring the collection - download the first chapter of every title for free.

New Journal of Physics

CrossMark

PAPER

Theory and modeling of electron fishbones

G Vlad[1], **V Fusco**[1], **S Briguglio**[1], **G Fogaccia**[1], **F Zonca**[1,2] **and X Wang**[3]

[1]   ENEA, Dipartimento FSN, C. R. Frascati, via E. Fermi 45, I-00044 Frascati (Roma), Italy
[2]   Institute for Fusion Theory and Simulation and Department of Physics, Zhejiang University, Hangzhou 310027, People's Republic of China
[3]   Max-Planck-Institut für Plasmaphysik, Boltzmannstrasse 2, D-85748 Garching, Germany

E-mail: gregorio.vlad@enea.it

Abstract

Internal kink instabilities exhibiting fishbone like behavior have been observed in a variety of experiments where a high energy electron population, generated by strong auxiliary heating and/or current drive systems, was present. After briefly reviewing the experimental evidences of energetic electrons driven fishbones, and the main results of linear and nonlinear theory of electron fishbones, the results of global, self-consistent, nonlinear hybrid MHD-Gyrokinetic simulations will be presented. To this purpose, the extended/hybrid MHD-Gyrokinetic code XHMGC will be used. Linear dynamics analysis will enlighten the effect of considering kinetic thermal ion compressibility and diamagnetic response, and kinetic thermal electrons compressibility, in addition to the energetic electron contribution. Nonlinear saturation and energetic electron transport will also be addressed, making extensive use of Hamiltonian mapping techniques, discussing both centrally peaked and off-axis peaked energetic electron profiles. It will be shown that centrally peaked energetic electron profiles are characterized by resonant excitation and nonlinear response of deeply trapped energetic electrons. On the other side, off-axis peaked energetic electron profiles are characterized by resonant excitation and nonlinear response of barely circulating energetic electrons which experience toroidal precession reversal of their motion.

1. Introduction

The mutual interaction of particle populations, characterized by very disparate kinetic energies, is of great interest for research on thermonuclear plasmas of fusion relevance, and, in particular, for the so-called 'ignited' plasmas, in which the 3.52 MeV α-particles, released in deuterium–tritium (D–T) reactions, have to thermalize by Coulomb collisions with the bulk thermal D–T plasma in order to self sustain its temperature. The interplay of fusion α-particles and magnetohydrodynamics (MHDs), Alfvénic-like modes has been recognized, since long time, as a crucial issue for the success of next generation, 'ignited' devices as, e.g., ITER [1]. Indeed, the potential enhancement of the radial transport of energetic particles (EPs) toward the edge of the plasma device while preventing them to fully thermalize could, in turn, degrade the fusion performance on one side, and damage the plasma facing components on the other. Similar phenomenology could also take place because of energetic particles accelerated by auxiliary heating systems, as, e.g., neutral beam (NB) injection and a variety of radio frequency heating and current drive systems, and, indeed, has been observed in a large selection of present days auxiliary heated toroidal plasma devices (see, e.g., [2, 3]).

One of the 'case studies' of EP driven MHD-like modes is the 'fishbone' mode, originally observed in the Poloidal Divertor eXperiment (PDX) [4] device, owing its name to the characteristic fishbone-like shape of the perturbed magnetic field signal evolution. The fishbone is an internal kink-like instability driven, in PDX, by energetic ions due to NB injection, which results in anomalous losses of energetic ions themselves. The theoretical interpretation in terms of resonant wave-particle interaction at the EP toroidal precession frequency was first proposed in [5] briefly after the experimental observations.

More recently, internal kink instabilities excited by supra-thermal electrons and exhibiting fishbone like behavior have been observed in the Doublet III-D (DIII-D) [6] device, where the high-energy electron population was generated by electron cyclotron (EC) current drive. Later on, other devices observed fishbone oscillations with electron heating only, i.e., electron cyclotron resonant heating (ECRH) and/or lower hybrid heating (LHH) and lower hybrid (LH) current drive (see next section 2 for a brief review of experimental evidence of electron fishbones, e-fishbones). Electron fishbones have linear dispersion relation and excitation mechanisms that are similar to those of energetic ion driven fishbones; moreover, fluctuation induced transport of magnetically trapped resonant particles, due to precession resonance, is expected to depend on energy and not mass of the energetic particles involved, because of the bounce averaged dynamic response [7]. Electron fishbones are characterized by a very small ratio between the resonant particle orbit width and the characteristic fishbone length scale ($\sim \delta\boldsymbol{\xi}_r$, the rigid radial kink-type displacement). This is also expected to be the case of ion fishbones in burning plasmas of fusion interest due to the large plasma current in these devices, while this condition is not realized for the energetic ions in present-day experiments. These analogies between e-fishbones in present-day devices and fishbones in burning plasmas provide a practical motivation for investigating these processes, in addition to the general interest of studying e-fishbones 'per se'.

In this paper, after briefly reviewing the experimental evidences of energetic electrons driven fishbones as observed in present toroidal devices in section 2, and the main results of linear and nonlinear theory of e-fishbones in section 3, the results of global, self-consistent, nonlinear hybrid MHD-Gyrokinetic simulations will be presented in section 4 [8]. In particular, the extended/hybrid MHD-Girokinetic code XHMGC, described in [9], will be used. The effects of considering kinetic thermal ion compressibility and diamagnetic response (in order to allow for an entirely novel treatment of enhanced inertia response [7, 10, 11] and ion Landau damping [12]), and kinetic thermal electrons compressibility, in addition to the energetic electron contribution, will be enlightened in linear dynamics analysis. Nonlinear saturation and energetic electron transport will also be addressed, making extensive use of Hamiltonian mapping techniques [13, 14]. In order to illustrate different nonlinear dynamics, both centrally peaked and off-axis peaked energetic electron profiles will be discussed. In particular, centrally peaked energetic electron profiles are characterized by resonant excitation and nonlinear response of deeply trapped energetic electrons. Meanwhile, barely circulating energetic electrons are identified as responsible of driving the e-fishbone mode and causing its nonlinear evolution for off-axis peaked energetic electron profiles. Final considerations will be given in section 5.

2. Experimental evidences of energetic electron driven fishbones

Fishbone oscillation driven by energetic ions have been observed for the first time in PDX [4] discharges heated by perpendicular NB injection, where a large $n = 1$ MHD mode was observed causing losses of energetic ions. Deeply trapped ions, in presence of a beam deposition profile peaked near the magnetic axis, were recognized to drive the mode [4, 5] because of resonant wave-particle interaction at the EP toroidal precession frequency $\bar{\omega}_d$. Fishbone oscillations driven by suprathermal ion population have been observed, since then, on many tokamak devices [2, 3, 15, 16]. Observations indicate that the mode propagates poloidally in the ion diamagnetic drift direction, and toroidally parallel to the EP precession velocity, thus having $\omega \simeq \omega_{\mathrm{res}} \simeq \bar{\omega}_{\mathrm{dh}}$ and $\omega_{*\mathrm{h}}/\omega \simeq \omega_{*\mathrm{h}}/\bar{\omega}_{\mathrm{dh}} > 0$, consistent with theoretical predictions for unstable modes [5] (see also section 3). Here, ω_{res} is the resonance frequency, the overbar $\bar{x}$ on the quantity 'x' indicates its bounce average, the diamagnetic frequency $\omega_{*s} = \mathbf{k} \cdot \mathbf{v}_{*s} = \mathbf{k} \cdot \frac{c\mathbf{B} \times \nabla p_s}{n_s e_s B^2} \simeq \frac{nq(r)}{r} \frac{c}{n_s e_s B} \frac{dp_s}{dr}$ and the toroidal drift frequency $\omega_{\mathrm{d}s} = \mathbf{k} \cdot \mathbf{v}_{\mathrm{d}s} \simeq \frac{nq(r)}{r} \frac{cE_s}{e_s BR}$, with $\mathbf{v}_{*s}$ the diamagnetic velocity, $\mathbf{v}_{\mathrm{d}s}$ the magnetic drift velocity, 's' indicating the particle species, n the toroidal mode number, E_s the energy of the single particle, n_s the density, p_s the pressure, e_s the electric charge, r the minor radius coordinate, B the magnetic field, $q(r)$ the safety factor, and the subscript 'h' refers to energetic ('hot') particles. It is worth noting that the ratio $\omega_{*\mathrm{h}}/\bar{\omega}_{\mathrm{dh}}$ does not depend on the sign of the electric charge e_s: thus, deeply trapped energetic electrons with a density profile peaked on-axis and of energy similar to that of energetic ions could be expected to drive a similar fishbone mode, propagating poloidally in the direction of the electron diamagnetic drift, i.e., opposite to the ion fishbone (although with some more unfavorable conditions [7], see section 3).

The first observation of fishbone oscillations driven by energetic electrons (e-fishbones) is reported almost two decades later in DIII-D [6]. In that experiment, strong MHD activity was observed in presence of NB ion heating, in conjunction with off-axis EC current drive and heating on high field side (HFS) and negative central shear equilibria with $q_{\mathrm{min}} \approx 1$. The fishbone oscillations were stronger when EC was applied on the HFS equatorial plane ($\theta_{\mathrm{res}} \approx \pi$, with θ_{res} the resonant poloidal angle of the EC wave absorption location), and decreased while decreasing θ_{res} toward $\theta_{\mathrm{res}} = \pi/2$. From the DIII-D experiment the following conclusions were derived: (1) from ray-tracing and Fokker–Planck calculations, it was shown that energetic electrons with hollow

radial density profile were generated slightly internal to the $q_{\min} = 1$ surface, with a substantial fraction of barely trapped particles (i.e., particles, which spend most of their time near the tips of their banana orbits, and are preferentially heated when $\theta_{\mathrm{res}} \approx \pi$); (2) the diamagnetic drift velocity of the energetic electrons (whose sign depends on $\mathrm{sign}(e_s)\nabla p_s$, with $\mathrm{sign}(e_s)$ and p_s the sign of the electric charge and pressure of species 's', respectively) is parallel to that of the on-axis peaked energetic ions produced by NBs; (3) the orbit averaged toroidal precession velocity (depending on $\mathrm{sign}(e_s)E_s$) of trapped energetic electrons, which is opposite to the one of the energetic ions for deeply trapped particles, reverses its sign when considering barely trapped particles [17, 18], thus becoming parallel to that of deeply trapped energetic ions. As a conclusion, barely trapped energetic electrons with inverted radial density profile could meet the instability condition $\omega_{*\mathrm{Ee}}/\omega \approx \omega_{*\mathrm{Ee}}/\bar{\omega}_{\mathrm{dEe}} > 0$ and drive a fishbone instability, in analogy with deeply trapped energetic ions with on-axis peaked radial density profile (here, the subscript 'Ee' stands for 'energetic electron'). Fishbone like fluctuations at higher frequency were also observed in COMPASS-D [19] driven by ECRH and LH.

Electron fishbones driven only by HFS off-axis (near $q = 1$) ECRH were observed also in HL-1M tokamak [20]; applying LH waves was found to enhance the fishbone, but only in conjunction with ECRH. Meanwhile, the observation of fishbone oscillations driven by only LH waves has been reported on FTU [7, 21, 22] and Tore Supra [23, 24].

A careful experimental analysis to characterize the direction of propagation of the electron fishbone mode has been performed on HL-2A tokamak [25–29], where mode frequency of energetic electron driven fishbones during off-axis ECRH on both HFS and low field side (LFS) was studied. In particular, in [25] barely circulating energetic electrons were considered responsible to drive electron fishbones during off-axis ECRH on the LFS, whereas both barely circulating and barely trapped energetic electrons were considered responsible to drive electron fishbones during HFS heating. More recently, an interesting link between nonlinear dynamics of fishbone fluctuations in NB heated discharges and non-local thermal electron heat transport has been demonstrated in HL-2A [30].

3. Linear and nonlinear theory of e-fishbones

The theoretical framework for analyzing linear and nonlinear fishbone dynamics has been recently reviewed in [31]. Here, we briefly summarize the analysis given therein, referring to original works for more in-depth discussions.

Fishbone linear stability and nonlinear evolution can be described by the general fishbone like dispersion relation (GFLDR) [32, 33]

$$\mathrm{i}|s|\Lambda = \delta\hat{W}_{\mathrm{f}} + \delta\hat{W}_{\mathrm{k}}. \tag{1}$$

Here, we have assumed fishbone fluctuations with toroidal mode number $n = 1$ and s denotes magnetic shear at the rational surface $r = r_s$, where the safety factor $q(r_s) = 1$. For convenience, we adopt straight magnetic field line toroidal flux coordinates (r, θ, ζ), with r the radial (magnetic flux) coordinate, while θ and ζ are periodic angular variables in poloidal and toroidal directions, respectively. In equation (1), Λ accounts for the kinetic/singular layer response at $r = r_s$, where the fishbone mode structure is sharply varying. When s at $r = r_s$ vanishes, the singular layer response must be suitably rewritten into a form similar to equation (1), which can be found in [31–33] and is assumed to be adopted if necessary. Such explicit form is not given explicitly here, since it is not needed in the discussion of the formal properties of the GFLDR. Meanwhile, terms on the right-hand side of equation (1) describe potential energy contributions from the regular region, separating fluid ($\delta\hat{W}_{\mathrm{f}}$) and kinetic ($\delta\hat{W}_{\mathrm{k}}$) responses consistently with the original approach in [5]. Explicit expressions for Λ, $\delta\hat{W}_{\mathrm{f}}$ and $\delta\hat{W}_{\mathrm{k}}$ are given in [31–33] and will be omitted here for brevity.

The kinetic/singular layer response Λ accounts for the structures of the shear Alfvén wave continuous spectrum including kinetic and geometry effects, e.g., continuum damping, neoclassical inertia enhancement and Landau damping [32]. Meanwhile, $\delta\hat{W}_{\mathrm{f}}$ represents the potential energy fluctuation due to the fluid thermal plasma response and the fluid/convective behavior of the EP component. Kinetic responses of thermal and supra-thermal plasma are accounted for by $\delta\hat{W}_{\mathrm{k}}$, which, e.g., describes instability drive by resonant wave particle interaction at

$$\omega = \omega_{\mathrm{res}} = n\bar{\omega}_{\mathrm{d}} + \ell\omega_{\mathrm{b}}, \tag{2}$$

for magnetically trapped particles; and

$$\omega = \omega_{\mathrm{res}} = n\bar{\omega}_{\mathrm{d}} + (n\bar{q} - m + \ell)\omega_{\mathrm{b}}, \tag{3}$$

for circulating particles. Here, (m/n) are (poloidal/toroidal) mode numbers, $\bar{\omega}_{\mathrm{d}} \equiv (\omega_{\mathrm{b}}/2\pi)\oint(\dot{\zeta} - q\dot{\theta})(\mathrm{d}\theta/\dot{\theta})$ is the definition of the toroidal precession frequency, $\omega_{\mathrm{b}} \equiv 2\pi(\oint\mathrm{d}\theta/\dot{\theta})^{-1}$ is the bounce/transit frequency for magnetically trapped/circulating particles and $\oint\mathrm{d}\theta/\dot{\theta}(...)$ is taken along a closed equilibrium particle orbit.

Furthermore $\bar{q} \equiv \oint q\,\mathrm{d}\theta / \oint \mathrm{d}\theta$ [34] and ℓ indicates the 'bounce' harmonics of the considered wave-particle resonance.

In linear theory, equation (1) predicts that fishbones can be excited by magnetically trapped EPs at the precession frequency [5]. Thus, for deeply trapped EPs with pressure profile peaked at the magnetic axis, fishbones above excitation threshold are expected to rotate in the EP diamagnetic direction, as observed originally [4]. For e-fishbones, this situation is experimentally more difficult to achieve as they require a particularly strong fast-electron source, due to the stronger continuum damping for modes rotating in the electron than in the ion diamagnetic direction [7]. In fact, most favorable excitation conditions for e-fishbones are off-axis peaked EP pressure profiles with modes rotating in the ion diamagnetic direction, consistent with equations (2) and (3) and $\ell = 0$ for barely trapped/barely circulating EPs affected by precession reversal [6]. The important role of finite $(\bar{q} - 1)$ for barely circulating EPs in equation (3) has been recently emphasized in [35]. In the following sections, we will numerically investigate both situations; i.e., the case of pressure profile peaked on axis and e-fishbone excited by deeply trapped EPs, as well as the off-axis peaked EP pressure profile case excited by barely trapped/circulating electrons.

When nonlinear physics is investigated, equation (1) can be cast as a nonlinear equation for the evolution of the fishbone amplitude and essentially fixed (linear) radial mode structure [31]. The nonlinear wave–wave and wave-EP interactions are dominated, respectively, by the nonlinear responses Λ^{NL} and $\delta\hat{W}_{\mathrm{k}}^{\mathrm{NL}}$ [31–33]. Both zonal flows and currents, i.e., in general zonal structures (ZSs), contribute to Λ^{NL} and are generated by the dominant $(m, n) = (1, 1)$ component of the fishbone mode [36]. Meanwhile, $\delta\hat{W}_{\mathrm{k}}^{\mathrm{NL}}$ is due to phase space ZS (PSZS), that is self-consistent nonlinear distortions in the EP distribution function having the same symmetry (spatial structure) of the underlying EP reference equilibrium [34]. In general, $\delta\hat{W}_{\mathrm{k}}^{\mathrm{NL}}$ and nonlinear dynamics of PSZS dominate over Λ^{NL} and ZS nonlinear response for sufficiently strong EP drive. However, the role of ZS becomes increasingly more important approaching the excitation threshold, and Λ^{NL} has to be considered on the same footing as $\delta\hat{W}_{\mathrm{k}}^{\mathrm{NL}}$ near marginal stability [31]. This transition in the nonlinear behavior is quantitatively affected by kinetic and geometry effects, such as neoclassical inertia enhancement, which must be taken into account for a proper description of the self-consistent nonlinear fishbone dynamics in toroidal fusion plasmas. In this work, for simplicity, we consider a sufficiently strong supra-thermal electron source and numerically investigate only the effect of $\delta\hat{W}_{\mathrm{k}}^{\mathrm{NL}}$ and nonlinear dynamics of PSZS [34].

Following [31, 34], and assuming deeply trapped resonant EPs with negligible orbit width and a rigid plasma displacement $\delta\boldsymbol{\xi}_{r0}$, the evolution equation for the EP PSZS can be cast as

$$
\begin{aligned}
\frac{\partial}{\partial t}F_0(t) \simeq {}& \mathrm{St}F_0(t) + S(t) + 2\left(\frac{\bar{\omega}_{\mathrm{d}}}{\omega_0(\tau)}\right) \\
&\times \frac{\partial}{\partial r}\left[\int_{-\infty}^{+\infty} \mathrm{e}^{-\mathrm{i}\omega t}\left(\frac{\partial\hat{F}_0(\omega)}{\partial r} - \frac{\omega_0}{\bar{\omega}_{\mathrm{d}}}\frac{\mathcal{E}}{R_0}\frac{\partial\hat{F}_0(\omega)}{\partial\mathcal{E}}\right)\right. \\
&\left.\times\frac{(\gamma - \mathrm{i}\omega) - (\bar{\omega}_{\mathrm{d}} - \omega_0)(\gamma/\omega_0)}{(\bar{\omega}_{\mathrm{d}} - \omega_0)^2 + (\gamma - \mathrm{i}\omega)^2}|\omega_0(\tau)|^2|\delta\boldsymbol{\xi}_{r0}|^2\mathrm{d}\omega\right].
\end{aligned}
\tag{4}
$$

Here, $\mathrm{St}F_0(t)$ and $S(t)$ denote collision and external source terms; and the PSZS $F_0(t)$ depends on velocity space variables $\mu = v_\perp^2/2B_0 + \cdots$ (the magnetic moment) and $\mathcal{E} = v^2/2$ (energy per unit mass) as well as r but, for conciseness of notation, only time dependence is indicated explicitly. Meanwhile, $\hat{F}_0(\omega) \equiv (2\pi)^{-1}\int_0^\infty \mathrm{e}^{\mathrm{i}\omega t}F_0(t)\mathrm{d}t$ denotes the Laplace transform. Furthermore, B_0 is the magnetic field on the magnetic axis at toroidal major radius $R = R_0$ and fishbone fluctuations are assumed to occur with the time dependent frequency $\omega_0(\tau) + \mathrm{i}\gamma(\tau)$. The τ notation instead of t explicitly refers to sufficiently slow time variation, such that $|\dot{\omega}_0| \ll |\gamma\omega_0|$ [34].

Equation (4) coupled with equation (1) via $\delta\hat{W}_{\mathrm{k}}^{\mathrm{NL}}$ give the description of the self-consistent nonlinear evolution of PSZS and fishbone oscillations [31]. This process is generally non-perturbative; that is, fishbone spatiotemporal structures affect EP transport and vice versa. It is worthwhile noting that fishbone spatiotemporal structures are evolving in time even though the radial mode structure remains close to a rigid plasma displacement. In fact, mode amplitude and frequency are changing in time, and influence the phase space structure of $F_0(t)$ due to the radial and velocity space dependence of the resonance conditions, equations (2) and (3). With non-perturbative EP response, nonlinear evolution is dictated by maximization of wave-particle power transfer, as discussed in [31, 34]. In particular, equation (4) suggests that PSZS evolution tries to preserve the resonance condition; i.e., that $|\ddot{\Theta}| \ll \gamma^2 \sim \tau_{\mathrm{NL}}^{-2}$, with Θ the wave-particle phase and τ_{NL} the characteristic nonlinear time [31, 34]. The ensuing frequency chirping is typically non-adiabatic; that is $|\dot{\omega}_0| \sim \gamma^2 \sim \tau_{\mathrm{NL}}^{-2}$ and, thus, resonant EP continuously enter and leave the resonance region since wave-particle trapping is suppressed, consistently with maximization of wave-particle power transfer. A given group of particles remains in resonance for a finite interaction time, τ_I, given by the condition

$$\int_0^{\tau_I} (\omega_0(\tau) - \omega_{\mathrm{res}})\mathrm{d}\tau \simeq \pi. \tag{5}$$

Due to phase locking ($|\ddot{\Theta}| \ll \gamma^2 \sim \tau_{\mathrm{NL}}^{-2}$), resonant interaction is preserved during effective mode amplification and is rapidly lost after residual resonance detuning has shifted the wave-particle phase by $\sim\pi$, similar to the slippage of resonant electrons with respect to a short free electron laser pulse [31, 34]. In this way, mode amplification can continue as resonant EPs continuously enter (and leave) the resonance region. Equation (5) corresponds to a finite interaction length, Δr_I, set by the distance traveled by the PSZS group velocity ($\sim\omega_0\delta\boldsymbol{\xi}_{r0}$) over τ_I [31, 34].

Strong fishbone excitation occurs when $\Delta r_I \sim r_s$; i.e., when resonant particles are convectively pumped out from within the $q(r_s) = 1$ magnetic flux surface as discussed in the original work by White *et al* [37]. In such a case, saturation corresponds to balancing the convective power loss with the wave-particle power transfer, yielding $|\delta\boldsymbol{\xi}_{r0}/r_s| \sim |\gamma/\omega_0|$ [31]. This behavior is demonstrated by present numerical simulation results with on axis peaked supra-thermal electron pressure profile, resonantly driven by deeply trapped particle at the precession resonance. For weaker EP drive and $\Delta r_I < r_s$, after a group of particles looses the resonance condition according to equation (5), a new group of particles can enter the resonance region because of non-adiabatic frequency chirping ($|\dot{\omega}_0| \sim \gamma^2 \sim \tau_{\mathrm{NL}}^{-2}$) and mode amplification can continue until it is suppressed by equilibrium non-uniformity [31, 34]. This behavior has been recently observed by numerical simulations based on a reduced description of the fishbone burst cycle that can be obtained from equations (1) and (4) with some additional simplifying assumptions [38].

When EP drive is further reduced, the effect of ZS should be considered on the same footing of PSZS nonlinear dynamics, as anticipated above. This is beyond the scope of the present work, where we focus on nonlinear wave-EP interaction and the effect of $\delta\hat{W}_{\mathrm{k}}^{\mathrm{NL}}$ only. Application of equations (1) and (4) in such a case, approaching marginal stability and with perturbative EP drive, yields the prediction fishbone saturation by local EP redistribution. In the case of supra-thermal electron pressure profile peaked off-axis, numerically analyzed in this work as illustration of e-fishbones driven by barely trapped/circulating EPs, ω_{res} radial profile has a local maximum at r_s, corresponding to slowly evolving (adiabatic) PSZS of $\Delta r_B \sim |2\omega_0/\omega_{\mathrm{res}0}''|^{1/3}|\delta\boldsymbol{\xi}_{r0}|^{1/3}$ radial extension, with $\omega_{\mathrm{res}0}''$ the second radial derivative of ω_{res} at r_s. It is then possible to show that fishbone saturation due to local EP relaxation occurs at $|\delta\boldsymbol{\xi}_{r0}| \sim \gamma^3|\omega_0|^{-3/2}|\Delta\omega|^{-3/2}|2\omega_0/\omega_{\mathrm{res}0}''|^{1/2}$, with $\Delta\omega = \omega_{\mathrm{res}0} - \omega_0$.

4. Numerical simulations

4.1. Description of XHMGC

In the following sections we will present the results of numerical simulations performed using the HMGC code [39–41], which is a hybrid [42] MHD gyrokinetic code originally developed at the Frascati Laboratories. In HMGC, the thermal plasma is described by $O(\epsilon^3)$ nonlinear reduced MHD equations [43], which describe circular shifted magnetic surface equilibria; moreover, the limit of zero bulk plasma pressure is also assumed; the energetic particles are described by nonlinear Vlasov equation in the drift-kinetic limit, solved using particle-in-cell technique, the two components (thermal and energetic particles) being coupled [42] via the pressure tensor term of the EP species entering in the extended momentum equation of the bulk plasma. The hybrid scheme allows to consider the effect of the energetic particles on the electromagnetic fields self-consistently, i.e., they are retained non-perturbatively: thus, the mutual effect of energetic particles and MHD-like modes (as, e.g., toroidal Alfvén modes, TAEs and internal kink modes), as well as modes which do not have their MHD counterpart (as, e.g., energetic particle driven modes, EPMs), can be studied properly; in particular, energetic particles will contribute to both time evolution of the mode (i.e., to the growth rate and frequency) and to its spatial structure (i.e., to the eigenfunction). HMGC has been extensively used to study TAEs and EPMs [41, 44, 45], as well as in the analysis of modes observed in existing devices (JT-60U [46], DIII-D [47]) or expected in forthcoming burning plasmas (ITER [48, 49]) and proposed experiments (FAST [50, 51]). The original version of HMGC has been recently extended to include new physics (XHMGC [9]): diamagnetic effects and thermal ion compressibility are retained in the extended momentum equation of the bulk plasma through the divergence of the thermal ion pressure tensor, obtained by solving the nonlinear Vlasov equation for that population, in order to account for enhanced inertia response [7, 10, 11] and ion Landau damping [12]. Moreover, XHMGC is able to treat simultaneously, using the kinetic formalism, up to three independent particle populations, assuming different equilibrium distribution functions (as, e.g., bulk ions and electrons, energetic ions and/or electrons accelerated by NB, ICRH, ECRH, fusion alphas, etc). The XHMGC code has been also used to simulate fishbone modes driven by energetic electrons [8]. With respect to energetic ion driven modes (as, e.g., TAEs and EPMs), the simulation of e-fishbones poses the challenge of properly follow the extremely fast parallel electron motion along equilibrium magnetic field lines, in order to correctly evaluate the effective bounce averaging during both linear and nonlinear dynamics. To this purpose, a suited sub-cycling scheme has been introduced and solved in

the particle-in-cell scheme. As synthetic diagnostic tool, XHMGC allows to follow, in a self-consistent simulation, a set of test particles; the phase-space coordinates of such particles are stored in time, and can be used to compute a variety of single particle physical quantities as , e.g., the single particle frequencies of the supra-thermal electrons, namely, the precession and bounce frequencies. The resonances underlying the linear instability can be clearly identified in this way. Furthermore, the use of EP phase-space diagnostics, based on Hamiltonian mapping techniques [13] generating kinetic Poincaré plots, allow us to isolate the physics processes underlying fishbone mode saturation, frequency chirping and secular (versus diffusive) EP redistribution.

The energetic electrons ('Ee') distribution function used in the following simulations is:

$$f_{\text{Ee}} \propto \frac{n_{\text{Ee}}(\psi)}{T_{\text{Ee}}(\psi)^{3/2}} \Xi(\alpha;\, \alpha_0,\, \Delta) e^{-E/T_{\text{Ee}}(\psi)}, \tag{6}$$

$$\Xi(\alpha;\, \alpha_0,\, \Delta) \equiv \frac{4}{\Delta\sqrt{\pi}} \frac{\exp\left[-\left(\dfrac{\cos\alpha - \cos\alpha_0}{\Delta} \right)^2 \right]}{\text{erf}\left(\dfrac{1 - \cos\alpha_0}{\Delta} \right) + \text{erf}\left(\dfrac{1 + \cos\alpha_0}{\Delta} \right)}, \tag{7}$$

where $E = m_e v^2/2 + M\omega_{\text{ce}}$ is the single particle energy, with v the parallel (to the equilibrium magnetic field) velocity, M the conserved magnetic moment (here defined as $M \equiv m_e v_\perp^2/(2\omega_{\text{ce}})$), and $\omega_{\text{ce}} = eB/(m_e c)$ the cyclotron frequency with e and m_e being the (absolute value of) charge and mass of electrons, respectively, and B the local equilibrium magnetic field. Moreover, $n_{\text{Ee}}(\psi)$ and $T_{\text{Ee}}(\psi)$ are the radial density and temperature profiles, respectively, ψ being the (normalized) poloidal flux ($\psi = 0$ on the magnetic axis and $\psi = 1$ at the plasma edge). The function $\Xi(\alpha;\, \alpha_0,\, \Delta)$ models the anisotropy in velocity space of the distribution function, with $\cos\alpha \equiv v/\sqrt{2E/m_e}$, $\sin^2\alpha \equiv M\omega_{\text{ce}}/E$, and α is the pitch angle of the energetic electrons. Within the code, the parallel velocity is normalized to the on-axis energetic electron thermal velocity $\hat{u} \equiv v/v_{\text{th,Ee,0}}$, with $v_{\text{th,Ee,0}} = \sqrt{T_{\text{Ee0}}/m_e}$, and the magnetic moment is normalized as $\hat{M} \equiv M\omega_{\text{ce0}}/T_{\text{Ee0}}$, with the subscript '0' indicating on-axis values.

In the following simulations performed with XHMGC, the contribution to Landau damping, enhanced plasma inertia (mostly due to trapped particles), finite compressibility of thermal ions, as well as Landau damping and finite compressibility of thermal electrons will be all treated kinetically by considering isotropic Maxwellian distribution functions with $n_{\text{th},j}(\psi)$, $T_{\text{th},j}(\psi)$ being the corresponding density and temperature profiles, with $j = i,\, e$. We will neglect mode-mode coupling nonlinearities, thus considering single n toroidal mode number simulations, while particles nonlinearities will be fully retained.

4.2. Energetic electrons with density profile peaked on-axis

As a first example of e-fishbone we will consider an energetic electron population with on axis peaked density profile. Similarly to the conventional energetic ion driven fishbones, deeply trapped energetic particles are expected to drive the mode. The same FTU-like equilibrium and scenario of [8] will be considered in this section, namely a torus of circular cross section with inverse aspect ratio $\epsilon = a/R_0 \approx 0.3$ (with a and R_0 the minor and major radius, respectively). The safety factor profile is slightly reversed, with $q_0 \approx 1.25$, $q_{\min} \approx 1.05$ at the surface $r_{q_{\min}}/a \approx 0.35$ and $q_a \approx 6$ (see figure 1, left). Reference on-axis magnetic field $B_0 = 5.4$ T, deuterium bulk plasma with on-axis density $n_{i0} = 1 \times 10^{20} m^{-3}$ and profile $n_i(\psi)/n_{i0} = (1 - \psi)^{1/2}$, on-axis ion temperature $T_{i0} = 2$ keV and radial profile $T_i(\psi)/T_{i0} = (1 - \psi)$ have been assumed as well (see figure 1, right); thus, $v_{\text{th,i,0}}/v_{A0} \approx 3.72 \times 10^{-2}$ (with $v_{A0} \equiv B_0/\sqrt{4\pi n_{i0} m_i}$ being the on-axis Alfvén velocity), while the on-axis bulk ion Larmor radius is $\rho_i/a \approx 4.27 \times 10^{-3}$. Bulk electrons have been assumed to have the same radial density and temperature profiles, with $n_{e0} = n_{i0}$ and $T_{e0} = 7$ keV; thus, $v_{\text{th,e,0}}/v_{A0} \approx 4.22$, while the on-axis bulk electron Larmor radius is $\rho_e/a \approx 1.32 \times 10^{-4}$. Energetic electrons described by a distribution function with perpendicular temperature much higher than the parallel one are considered in the simulations by assuming $\cos\alpha_0 = 0$ and $\Delta = 0.1$, see equation (7), in order to maximize the fraction of trapped particles, which are expected to contribute to the resonant excitation of electron fishbone mode; the energetic electron density radial profile is $n_{\text{Ee}}(\psi) = n_{\text{Ee0}} \exp(-10\psi)$, whereas the energetic electron temperature is assumed to be uniform $T_{\text{Ee}} = T_{\text{Ee0}} = 50$ keV (see figure 1, right); thus, $v_{\text{th,Ee,0}}/v_{A0} \approx 12.27$, while the on-axis energetic electrons Larmor radius is $\rho_{\text{Ee}}/a \approx 3.52 \times 10^{-4}$. This equilibrium has been already analyzed in [8], were it was shown that the electron fishbone mode was destabilized above a certain threshold energetic electron density, propagating poloidally in the direction of the energetic electron diamagnetic velocity (which is, for this equilibrium, also parallel to the bulk electron diamagnetic velocity), and excited by resonance with deeply trapped energetic electrons. Here, we will reconsider the linear results presented in [8], where the kinetic contribution of the energetic electrons and bulk ion was considered, by also adding the kinetic contribution of bulk electrons. Moreover, a novel nonlinear analysis using test particles Hamiltonian mapping (TPHM) techniques [13, 14] will allow us to illuminate the nonlinear saturation and radial transport associated with such mode.
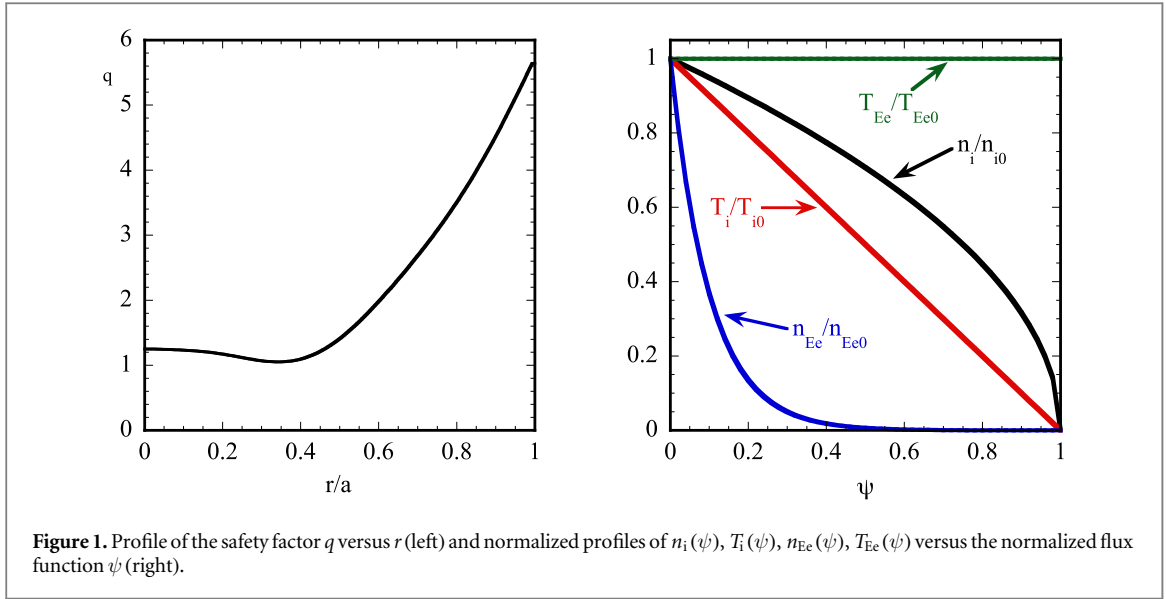
Figure 1. Profile of the safety factor *q* versus *r* (left) and normalized profiles of $n_i(\psi)$, $T_i(\psi)$, $n_{Ee}(\psi)$, $T_{Ee}(\psi)$ versus the normalized flux function ψ (right).
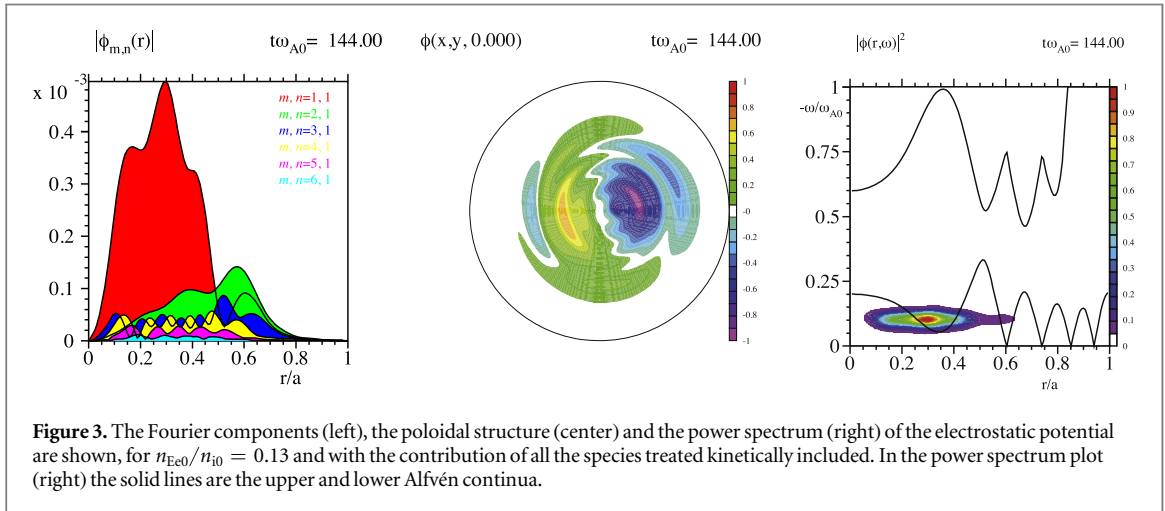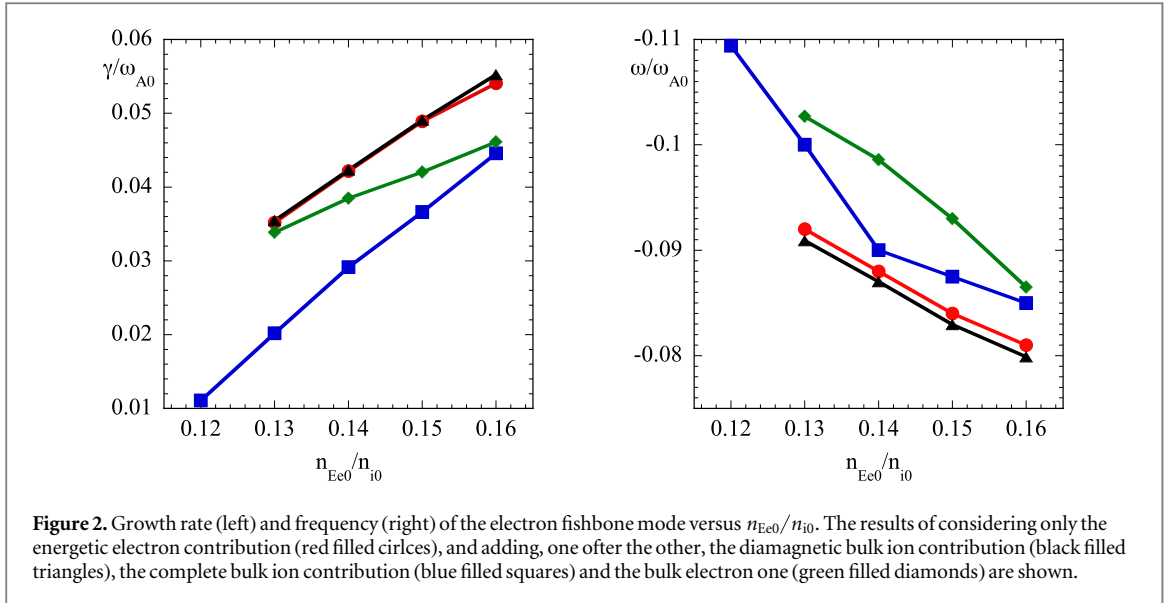
4.2.1. Linear dynamics

In this section we will investigate the relative importance of different driving and damping processes accounted for in the model, i.e., energetic electrons compressibility, thermal ion compressibility and diamagnetic effects, and thermal electron compressibility. Following [9], where the model implemented in XHMGC has been described in detail, let us consider the perpendicular component of the extended MHD momentum equation:

$$
\rho_b \left[\frac{\partial}{\partial t} + \left(\underbrace{\frac{\mathbf{b} \times \nabla P_{0i\perp}}{\rho_i \omega_{ci}}}_{\text{diamagnetic, bulk ions}} + \delta\mathbf{v}_b \right) \cdot \nabla \right] \delta\mathbf{v}_b
$$
$$
= - \underbrace{(\nabla \cdot \mathbf{P}_e)_\perp}_{\text{bulk electrons}} - \underbrace{(\nabla \cdot \mathbf{P}_i)_\perp}_{\text{bulk ions}} - \underbrace{(\nabla \cdot \mathbf{P}_{Ee})_\perp}_{\text{energetic electrons}}
$$
$$
+ \left(\frac{\mathbf{J} \times \mathbf{B}}{c} \right)_\perp,
$$

(8)

where $\delta\mathbf{v}_b$ is the perturbed velocity ($\propto \delta\mathbf{E} \times \mathbf{B}$) of the bulk ions, ρ_i is the bulk ion Larmor radius, ω_{ci} is the ion cyclotron frequency and ρ_b is the mass density $\rho_b = m_i n_i$ of the bulk ions. In equation (8) the diamagnetic bulk ion contribution, and the different kinetic contributions coming from the energetic electrons, bulk ions and bulk electrons have been explicitly indicated. In the following simulations the toroidal mode number is $n = 1$, the poloidal Fourier components retained are $m = 1, \ldots, 6$, normalized resistivity $S^{-1} = 3 \times 10^5$ and viscosity $\nu\tau_{A0}/a^2 = 3 \times 10^{-8}$ have been considered to ensure numerical stability (here S is the Lundquist number $S \equiv 4\pi a^2/(\eta c^2 \tau_{A0})$, $\tau_{A0} = R_0/v_{A0}$ being the on axis Alfvén time, η the resistivity, and $\omega_{A0} \equiv \tau_{A0}^{-1}$ the on axis Alfvén frequency). In figure 2 the results of a scan in which the strength of the energetic electrons driving term $(\nabla \cdot \mathbf{P}_{Ee})_\perp$ (which is $\propto n_{Ee0}/n_{i0}$) is varied are presented, showing the dependence of the growth rate and the frequency of the electron fishbone mode on the strength of the drive. Several curves are shown in figure 2, corresponding to switching on, one after the other, the contributions isolated in equation (8). First, only the divergence of the energetic electron pressure tensor $(\nabla \cdot \mathbf{P}_{Ee})_\perp$ is retained, then also the diamagnetic bulk ion term $(\mathbf{b} \times \nabla P_{0i\perp})/(\rho_i\omega_{ci})$ is added and, subsequently, the divergence of the thermal ion pressure tensor $(\nabla \cdot \mathbf{P}_i)_\perp$, which account for the thermal ion Landau damping and generalized inertia, retaining consistently the actual dynamic response of trapped and circulating thermal ions (see also section 2.2 and appendix A of [7]). Finally, the divergence of the thermal electron pressure tensor $(\nabla \cdot \mathbf{P}_e)_\perp$ is also included. The contribution of energetic electrons drives the mode, which has a clear internal kink characteristic with a dominant $m = 1$ component localized, in radius, approximately inside the q_{min} surface $r_{q_{min}}/a \approx 0.35$ (see figure 3 left); the poloidal structure (see figure 3 center) rotates in counter clock wise direction, which corresponds to a mode propagating in the (bulk and energetic) electron diamagnetic velocity direction resulting in a negative real frequency (see figure 3 right), considering the standard fast Fourier conventions used for extracting the frequency spectra from the time dependent solution of the unknown fields (the e.s. potential ϕ and the parallel component of the vector potential A) as obtained by the initial value code XHMGC. Referring to the results shown in figure 2, we observe that the growth rate increases almost linearly with the strength of the drive, $\propto n_{Ee0}/n_{i0}$, and the frequency (in absolute value) slightly decreases. When considering also the diamagnetic bulk

Figure 2. Growth rate (left) and frequency (right) of the electron fishbone mode versus n_{Ee0}/n_{i0}. The results of considering only the energetic electron contribution (red filled circles), and adding, one ofter the other, the diamagnetic bulk ion contribution (black filled triangles), the complete bulk ion contribution (blue filled squares) and the bulk electron one (green filled diamonds) are shown.

Figure 3. The Fourier components (left), the poloidal structure (center) and the power spectrum (right) of the electrostatic potential are shown, for $n_{Ee0}/n_{i0} = 0.13$ and with the contribution of all the species treated kinetically included. In the power spectrum plot (right) the solid lines are the upper and lower Alfvén continua.

ion term, very little variation is observed, both in growth rate and frequency: indeed, the absolute value of this term, evaluated at its maximum radial position ($r/a \approx 0.35$) is much less (by a factor ≈ 30) than the absolute value of the frequency of the mode. When adding the term $(\nabla \cdot \mathbf{P}_i)_\perp$, on the contrary, the growth rate of the mode is notably reduced, showing as the effect of considering the thermal ion Landau damping and enhanced inertia increases the threshold in n_{Ee0}/n_{i0} required to destabilize the mode; also the absolute value of the frequency of the mode increases. Finally, when adding the term $(\nabla \cdot \mathbf{P}_e)_\perp$ which accounts for the bulk electrons, an increase of the growth rate is observed, which diminishes its importance as n_{Ee0}/n_{i0} is increased. Note that the positive contribution to the growth rate of the bulk electrons appears only if the electron fishbone is already driven unstable, indeed in absence of the energetic electrons the system is still stable.

Some more insight on the linear dynamics of the electron fishbone driven by energetic electrons with density profile peaked on-axis can be gained considering the power exchange between the various particle species and the wave. In figure 4 the power exchange in the (v, M) space is shown, for several radial shells, in a simulation in which the kinetic contributions of all the particle species are retained. The dominant drive contribution comes from the deeply trapped energetic electrons (the solid and dashed curves in each plot refer to the approximative boundary between trapped and circulating region in the phase space, for the inner (solid curve) and outer (dashed curve) radii of the radial shell considered, respectively). Note that in the plots shown in figure 4 the normalized parallel velocity u refers to the parallel velocity the simulation markers ('macro-particles') have when crossing the equatorial plane at the poloidal angle $\theta = 0$; in particular, for trapped particles, the external 'leg' of the 'banana' orbit is chosen. Let us first consider the power exchange relative to the energetic electrons: as already stated in [8], the drive is given by the deeply trapped electrons, figure 4, upper-left plot. Making use of the test particle Hamiltonian mapping techniques [14], we can gain some insight on the characteristic resonances of the energetic electrons. As stated in section 4.1, the code HMGC can be used to evolve a set of test particles in the
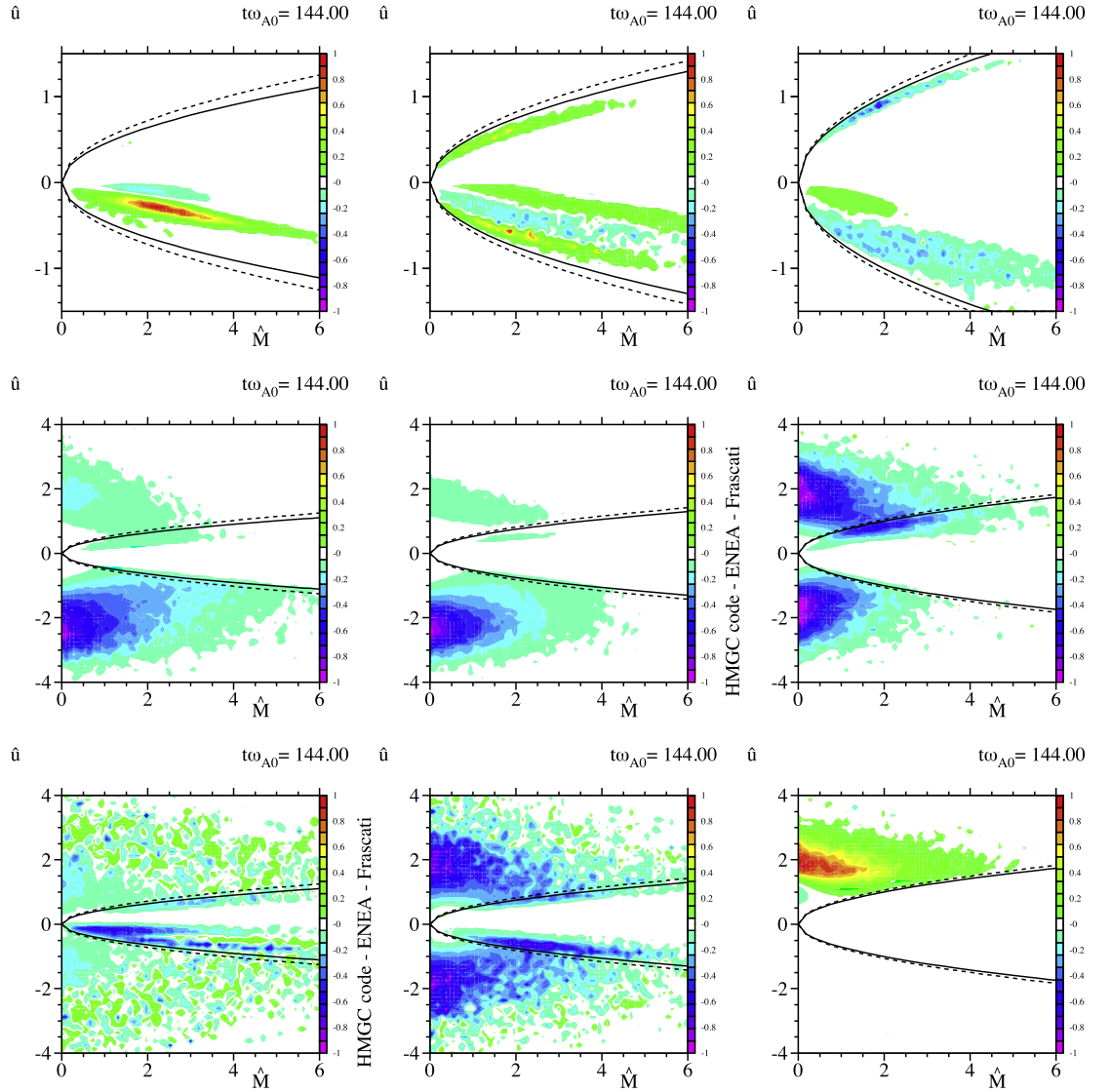
Figure 4. Power exchanges between particles and wave (red to green colors refer to power from the particles to the wave, light blue to purple refer to power from the wave to the particles; color scale is relative to each frame) in the normalized $(\hat{u} \equiv v/v_{th,s,0}, \hat{M} \equiv M\omega_{cs0}/T_{s0}$, with $s = $ Ee, i, e) space are shown for the energetic electrons (top row), bulk ions (center row) and bulk electrons (bottom row); three radial shells are considered: $0.17 \lesssim r/a \lesssim 0.22$ (left), $0.23 \lesssim r/a \lesssim 0.28$ (center), $0.442 \lesssim r/a \lesssim 0.47$ (right).

time dependent e.m. fields computed by a self-consistent simulation [14]. A suitable choice will be to choose the set of test particles as the ones with strongest resonance with the wave during linear growth phase. This can be done by choosing the particles which belong to the phase space region where the maximum power exchange between energetic particles and wave occurs (see, e.g., figure 4). Once the coordinates of such a region have been selected (i.e., $r = r_0$, $M = M_0$, $v = v_{\parallel,0}$), we can define, following [13, 14], the quantity $C \equiv \omega_0 P_\phi - nE$, with $P_\phi \equiv m_s R_0 B_0 v/B + e_s R_0 (\psi - \psi_0)/c$ being the canonical toroidal angular momentum. The quantity C is a constant of the (perturbed) motion, provided that the perturbed field is characterized by a single toroidal mode number n and a constant frequency. At the leading order [14], we can approximate $P_\phi \simeq m_s R v + e_s R_0 (\psi_{eq} - \psi_{eq,0})/c \equiv P_\phi(r, \theta, v)$, and $C \equiv \omega_0 P_\phi - n(m_s v^2/2 + M\omega_{cs}) \equiv C(r, \theta, M, v)$ (here, ψ_{eq} is the equilibrium poloidal flux function). Thus, the initial ($t = 0$) coordinates of the test particles can be chosen by varying (r, v) under the condition that $M = M_0$ and $C = C_0$; moreover, $\theta = 0$ and equispaced values of ϕ in the interval $[0, 2\pi[$ are also assumed. Figure 5 shows the results obtained during the linear growth phase of the simulation for a set of particles with $C = C_0$ and $M = M_0$, with C_0 and M_0 which corresponds to the maximum power exchange between energetic electrons and wave ($\theta = 0$, $r/a = 0.195$, $\hat{M} = 3$, $\hat{u} = -0.328$, and $\omega_0/\omega_{A0} \approx -0.1$, see figure 4): indeed, the resonant condition for trapped particles $\omega_0 = \omega_{res}(r) = n\bar{\omega}_d(r) + \ell\omega_b(r)$, for $n = 1$, $\ell = 0$ (with ℓ denoting the 'bounce harmonics'), is satisfied in correspondence of the peak of the power exchange between the (test) energetic electrons and wave, confirming
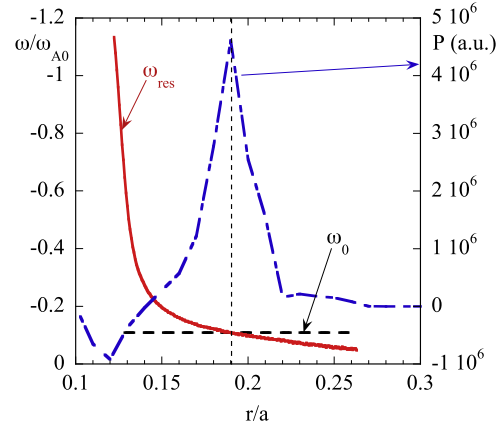
Figure 5. Radial dependence of the resonant frequency $\omega_{res}(r) = n\bar{\omega}_d(r)$ of the energetic electron test particles (solid red curve) compared with the mode frequency ω_0(dashed black line). Over imposed is the radial dependence of the test particle power exchange, (blue dotted–dashed curve).
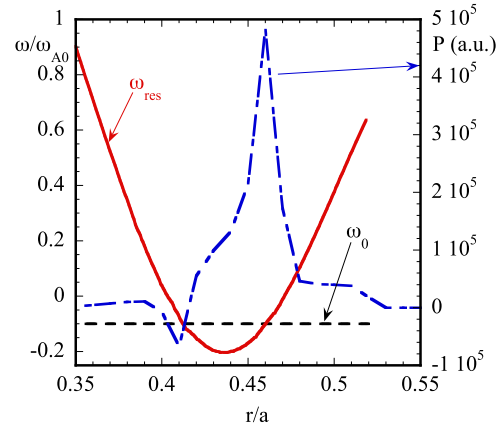

Figure 6. Radial dependence of the co-passing resonant frequency $\omega_{res}(r) = n\bar{\omega}_d(r) + (\bar{q} - 1)\omega_b$ of the bulk electron test particles (solid red curve) compared with the mode frequency ω_0(dashed black line). Over-imposed is the radial dependence of the test particle power exchange, (blue dotted–dashed curve).

that the precession frequency $\bar{\omega}_d$ of deeply trapped energetic electrons is driving the mode. Note also that the radial profile of the test particles resonant frequency $\omega_{res}(r)$, after a strong variation with radius for $r/a \lesssim 0.15$, is quite flat and close the value of the (linear phase) mode frequency ω_0: this feature will be relevant for the evolution of the mode during nonlinear saturation (see section 4.2.2).

From figure 4 the bulk ions are shown to contribute to the damping of the mode, mainly with co- and counter-passing particles, whereas the bulk electrons, depending on the radial shell considered, contribute to damping the mode with both passing and trapped particles in the internal radial shells, but strengthen the drive some where outside the q_{min} radius. Indeed, applying the same TPHM technique used above, it is possible to show that, in correspondence with the positive contribution of the bulk electrons in the radial shell $r/a \approx 0.46$, which exhibit a maximum for the power exchange at $\hat{M} \approx 0$ and $\hat{u} \approx 2.375$, it exists a radial double resonance with co-passing bulk electrons $\omega_0 = \omega_{res} = n\bar{\omega}_d + [\ell + (n\bar{q} - m)\sigma]\omega_b$, for $n = 1, m = 1, \ell = 0$, $\sigma = \text{sign}(v)$ and $\bar{q}$ the average of the safety factor over the particle orbit (see figure 6). Similarly, for the bulk ions, in the radial location where the damping is maximized ($r/a \approx 0.28$, $\hat{M} = 0.$ and $\hat{u} - 2.5$), a resonance can be found with counter-passing particles $\omega_0 = \omega_{res} = n\bar{\omega}_d + [\ell + (n\bar{q} - m)\sigma]\omega_b$, for $n = 1$, $m = 1, \ell = -2$.

4.2.2. Nonlinear dynamics

In the present section we will consider the nonlinear dynamics of the electron fishbone driven by energetic electrons with density profile peaked on-axis. We will refer, in this section, to a set of simulations in which only the contribution of the thermal ions treated kinetically will be considered beside the one of the energetic electrons, neglecting thus the kinetic response by thermal electrons, as in the case of the simulations presented in
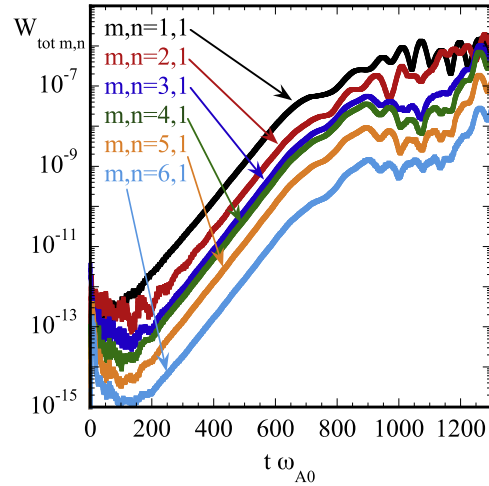
Figure 7. Total (kinetic plus magnetic) volume integrated MHD energies $W_{\text{tot};m,n}$ for the various Fourier components considered in the simulation are shown, for the case of $n_{\text{Ee0}}/n_{\text{i0}} = 0.12$.
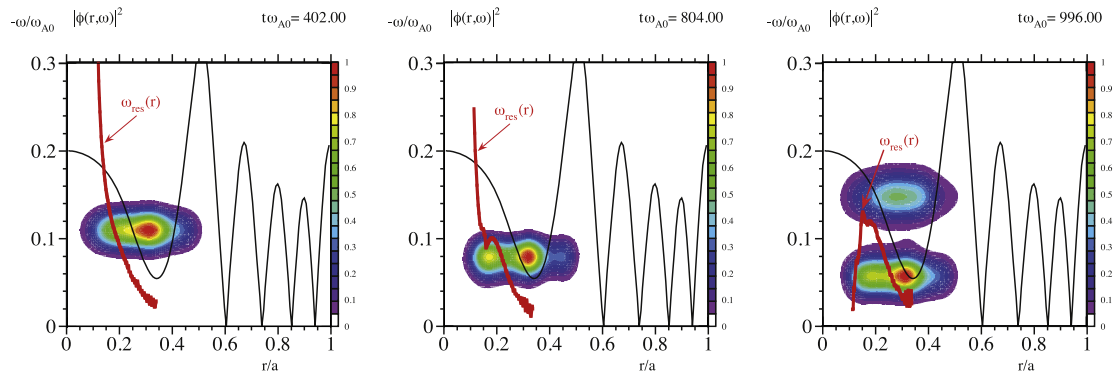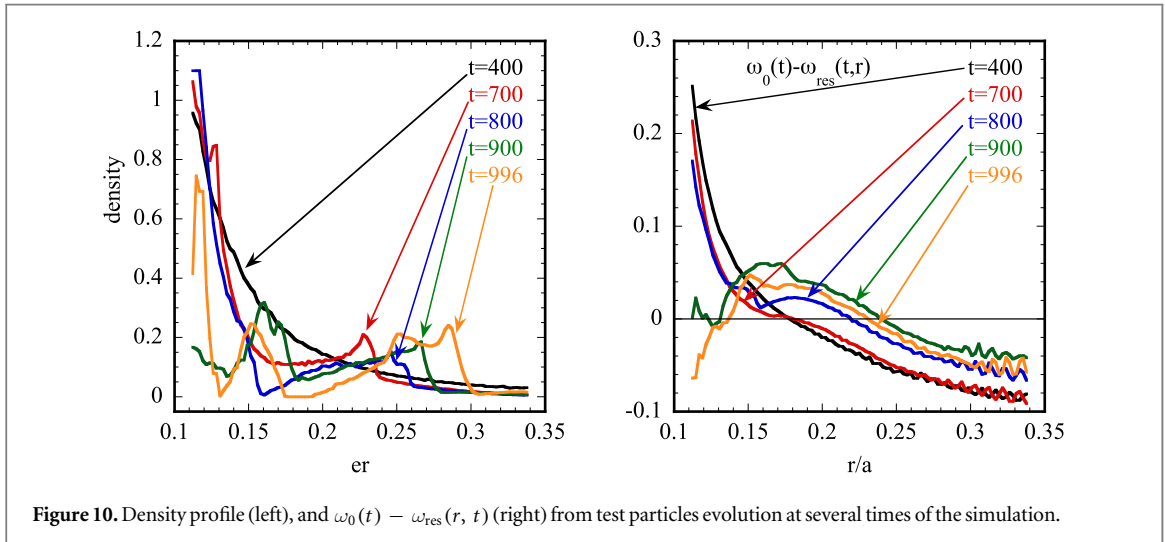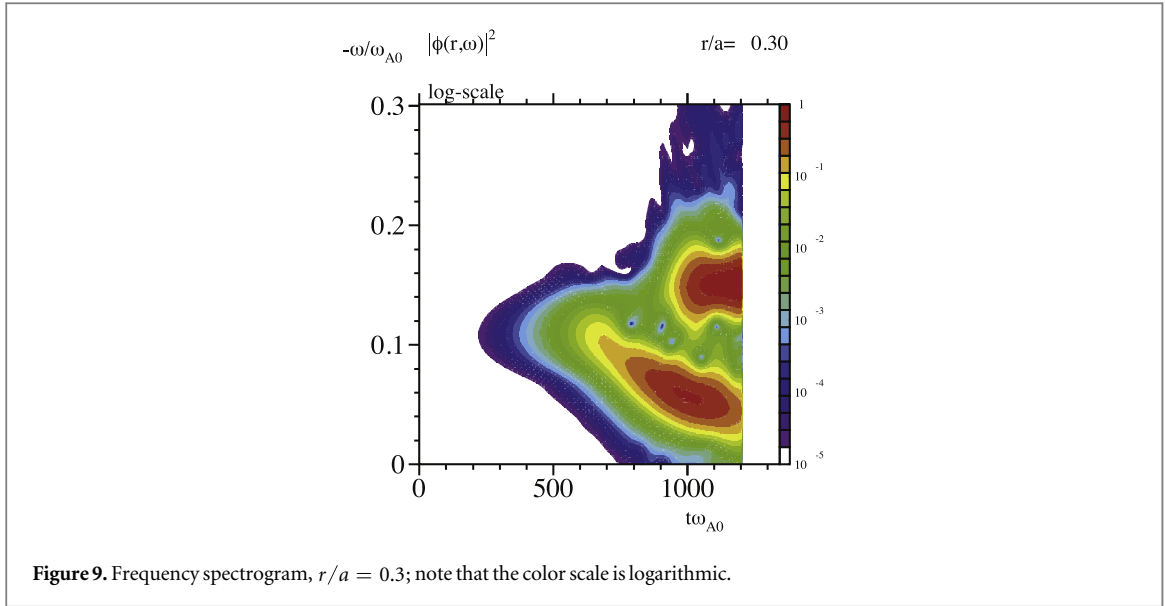

Figure 8. Frequency spectra of the electrostatic potential $\varphi(r, \omega)$ at several times (during linear phase, end of the earlier phase of saturation, late saturation); over imposed is the resonant frequency $\omega_{\text{res}}(r; C_0, M_0)$ of the test particles.

[8]. In figure 7 the time evolution of the total (kinetic plus magnetic) volume integrated MHD energies $W_{\text{tot};\,m,n}$ for the various Fourier components considered in the simulation are shown, for the case of $n_{\text{Ee0}}/n_{\text{i0}} = 0.12$ (the weakest simulation shown in figure 2).

As already discussed in [8], the saturation is characterized by a pronounced downward (in absolute value) frequency chirping, as it is shown in figure 8, where the frequency spectra of the electrostatic potential $\varphi(r, \omega)$ are shown at several times of the simulation (during linear phase ($t\omega_{A0} \approx 400$), end of the earlier phase of saturation ($t\omega_{A0} \approx 800$), late saturation ($t\omega_{A0} \approx 1000$)). In figure 8, superimposed on the frequency spectra, the instantaneous resonant frequency $\omega_{\text{res}} = \omega_{\text{res}}(r, t; C_0, M_0)$ is also reported: it is worthwhile noting that the instantaneous resonant frequency $\omega_{\text{res}}(r, t)$ changes in time, being always close to the local lower Alfvén continuum, and that the radial extension of the power spectrum $|\varphi(r, \omega)|^2$ is almost unchanged during the downward (in absolute value) chirping, as a consequence of the stiffness of radial shape of the internal kink eigenfunction. Furthermore, the mode, although chirping down, is always superimposed to the instantaneous $\omega_{\text{res}}(r, t)$ curve, thus suggesting phase-locking with the energetic particles identified by $C = C_0$, $M = M_0$.
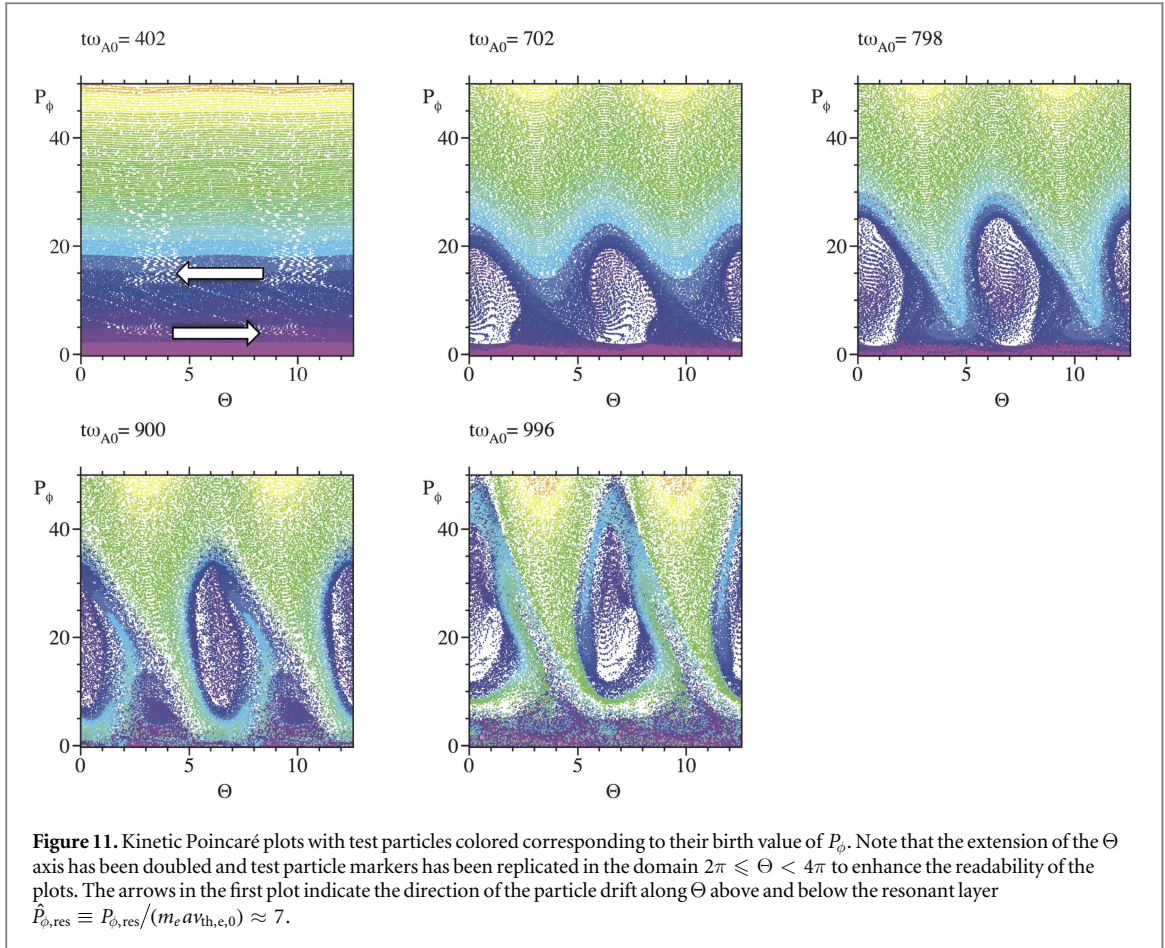
In figure 9 the spectrogram of the mode is shown at the radial location where the electrostatic potential has its peak: the frequency chirps down (in absolute value) as the simulation leaves the exponential growth of the linear phase (for $t\omega_{A0} \gtrsim 600$, see figure 7). In the subsequent strongly nonlinear regime ($t\omega_{A0} \gtrsim 1000$) a second dominant frequency appears ($|\omega/\omega_{A0}| \approx 0.15$), in correspondence to bursts observed in the total MHD energy.

By following the same set of test particles considered in section 4.2.1 also in the nonlinear phase of the simulation, we can further investigate the saturation mechanism of the mode and the associated radial transport of resonant particles. In figure 10 (left) the radial density profiles of the test particles are shown, for several times during the simulation ($t\omega_{A0} = 400$, during the linear growth phase, and $t\omega_{A0} = 700, 800, 900, 996$, during the saturation phase). Radial flattening is strongly evident in these resonant particles, starting at the radial position

Figure 9. Frequency spectrogram, $r/a = 0.3$; note that the color scale is logarithmic.

Figure 10. Density profile (left), and $\omega_0(t) - \omega_{\mathrm{res}}(r, t)$ (right) from test particles evolution at several times of the simulation.

where the power exchange between energetic particles and wave is stronger ($r/a \approx 0.185$, see figure 5). It is worthwhile noting that this strong radial transport of the energetic particles can become much less evident after averaging (summing) over the total (resonant plus non-resonant) EP radial density profile. From figure 10 (left) it can also be observed that the flattening of the radial profile, that starts at time $t\omega_{A0} \approx 600$ around $r/a \approx 0.185$, propagates inward, up to $r/a \approx 0.1$, and outward, up to $r/a \approx 0.3$. In figure 10 (right) the curves $\omega_0(t) - \omega_{\mathrm{res}}(r, t)$, as computed from the test particle evolution are shown, at several times during the simulation: the intersections of the curves with the reference zero line identify the resonance radial location. Until $t\omega_{A0} = 700$ the radial location of the resonance is almost unchanged ($r/a \approx 0.185$), as is the shape of the curve $\omega_0(t) - \omega_{\mathrm{res}}(r, t)$, which just begin to flatten around the resonant radius. At later times ($t\omega_{A0} = 800, 900, 996$), the instantaneous resonance frequency profile $\omega_0(t) - \omega_{\mathrm{res}}(r, t)$, as computed from the test particles evolution, continues to flatten in radius with respect to the linear phase and extends outward, but also, because of the frequency chirping of the mode, it shifts up: as a consequence, the resonant radius moves outward, i.e., toward higher values of the canonical toroidal angular momentum P_ϕ. In figure 11 the kinetic Poincaré plots are shown for the same times of simulation of figure 10 with test particles colored accordingly to their initial P_ϕ value: here, whenever a test particle completes a full banana or transit orbit in the poloidal plane at $t = \hat{t}$, by crossing the outer equatorial plane ($\theta = 0$), the corresponding values of the canonical toroidal angular momentum $P_\phi(\hat{t})$ and the wave-particle phase $\Theta(\hat{t})$ are computed, with $\Theta(\hat{t}) = \int^{\hat{t}} \omega_0(t)\mathrm{d}t - n\phi(\hat{t})$ and ϕ being the toroidal angle. Each test particle position in the plane (Θ, P_ϕ) is then updated by moving the marker in the 'kinetic Poincaré' plot [13]. The extremes of the vertical axis $P_\phi = [-0.13, 50]$ correspond to,
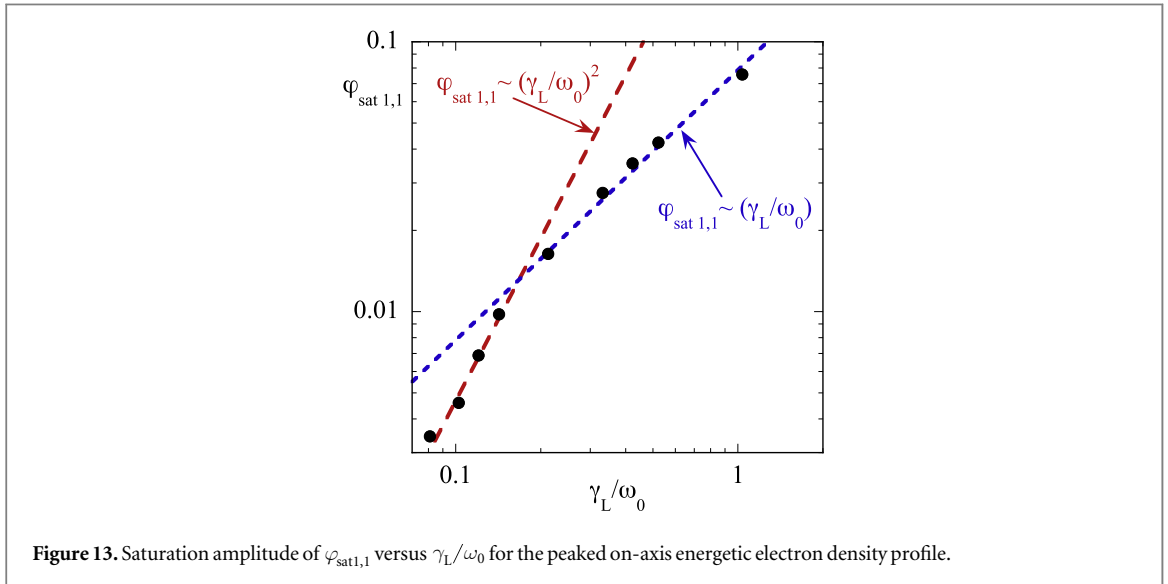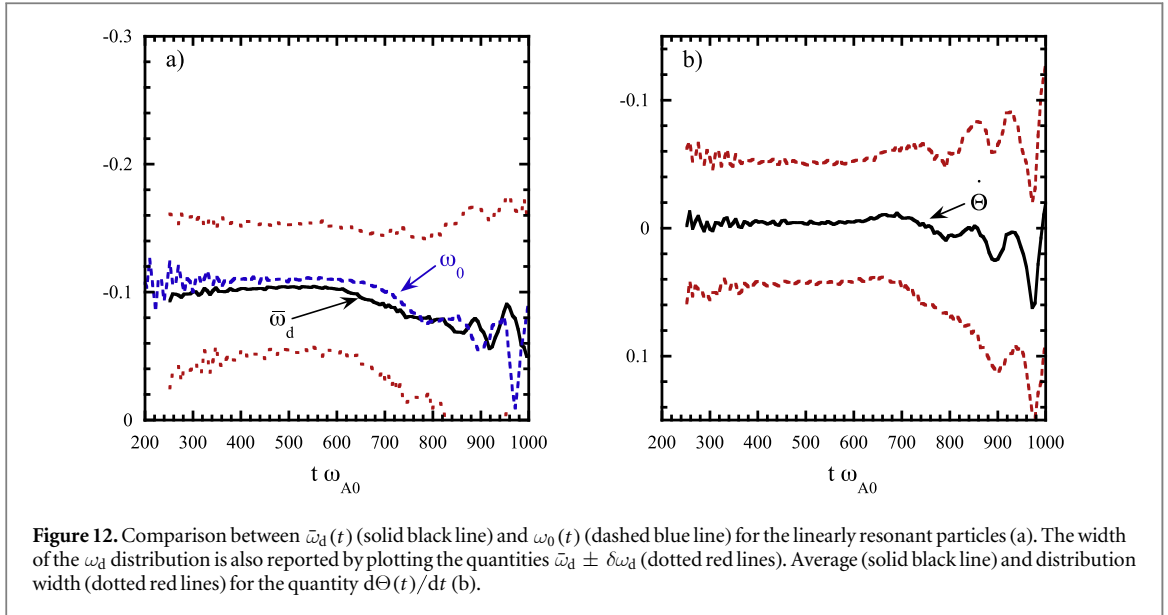
Figure 11. Kinetic Poincaré plots with test particles colored corresponding to their birth value of P_ϕ. Note that the extension of the Θ axis has been doubled and test particle markers has been replicated in the domain $2\pi \leqslant \Theta < 4\pi$ to enhance the readability of the plots. The arrows in the first plot indicate the direction of the particle drift along Θ above and below the resonant layer $\hat{P}_{\phi,\mathrm{res}} \equiv P_{\phi,\mathrm{res}}/(m_e a v_{\mathrm{th,e},0}) \approx 7$.

approximately, $r/a \approx [0.1, 0.3]$. Resonant particles during linear phase have their normalized $\hat{P}_\phi \equiv P_\phi/(m_e a v_{\mathrm{th,e},0}) = \hat{P}_{\phi,\mathrm{res}} \approx 7$ (violet/dark blue color), which corresponds, approximately, to $r_{\mathrm{res}}/a \approx 0.185$. During the linear phase of the simulation, when the perturbed e.m. fields are small, these resonant particles are fixed points in time in the space (Θ, P_ϕ), while particles with different values of their P_ϕ just drift toward higher or lower Θ, according to $\dot{\Theta} \approx \omega_0 - \omega_{\mathrm{res}}$, while keeping P_ϕ constant (see the arrows in the first frame of figure 11, indicating the drift direction along Θ in the two regions of P_ϕ). Once the e.m. fields have reached a sufficient high level, particles begin to be displaced in P_ϕ (due to $\mathbf{E} \times \mathbf{B}$ drift) also drifting along Θ (see figure 11, $t\omega_{A0} = 700$). When the sign of the perturbed field is inverted, $\partial P_\phi/\partial t$ changes its direction and if particles cross the $P_\phi = P_{\phi,\mathrm{res}}$ line, they invert their drift along Θ, beginning to roll in the wave (being eventually trapped in the wave itself). Particles that instead do not cross the $P_\phi = P_{\phi,\mathrm{res}}$ line, only oscillate in P_ϕ without inverting their drift along Θ (passing particles in the kinetic Poincaré plots nomenclature). In our simulation, because of the chirping mode, i.e., $\omega_0 = \omega_0(t)$ and of the dynamic modification of the radial profile of the resonant frequency $\omega_{\mathrm{res}} = \omega_{\mathrm{res}}(r, t)$, the resonant particles that are displaced at larger P_ϕ (because of $\mathbf{E} \times \mathbf{B}$ drift), will, in turn, continue to drift outward (instead of drifting horizontally in Θ, and reversing their motion toward the resonant layer when feeling a change of sign of the $\mathbf{E} \times \mathbf{B}$ drift). This outward drift gives rise (see figure 11, $t\omega_{A0} = 700, 800, 900, 996$) to vertical elongated structures, i.e., to a large radial transport of energetic resonant particles (see also the almost flat test particle density profiles for the same times in figure 10 (left)), consistent with the theoretical analysis given in section 3 [31, 34]. This process ends when the flattening of the test particle density profile approaches the q_{min} radius, where the internal kink eigenfunction sharply decreases ('radial decoupling', see [14]); it has to be noted that very little variation is observed in time on the shape of the eigenfunction, being the internal kink type eigenfunction quite stiff.

Evidence of phase locking is shown in figure 12, where the average of the precession frequency $\bar{\omega}_\mathrm{d}(t)$ of the linearly resonant particles, weighted with their power transfer during linear phase is shown, together with the width of its distribution (see [8]), and compared with the time varying (chirping) frequency of the mode (see figure 9). Also, the mode adjusts its frequency (thus keeping $|\dot{\Theta}| \approx 0$, the 'phase-locking' condition) in order to remain 'tuned' with the resonant particles which, meanwhile, experience their outward displacement.

Finally, we plot in figure 13 the saturation amplitude of the $m = 1$, $n = 1$ Fourier component of the electrostatic potential $\varphi_{\mathrm{sat}\,1,1}$ as the strength of the EP linear drive varies. For the saturation amplitude, we took

Figure 12. Comparison between $\bar{\omega}_d(t)$ (solid black line) and $\omega_0(t)$ (dashed blue line) for the linearly resonant particles (a). The width of the ω_d distribution is also reported by plotting the quantities $\bar{\omega}_d \pm \delta\omega_d$ (dotted red lines). Average (solid black line) and distribution width (dotted red lines) for the quantity $d\Theta(t)/dt$ (b).

Figure 13. Saturation amplitude of $\varphi_{sat1,1}$ versus γ_L/ω_0 for the peaked on-axis energetic electron density profile.

the maximum value of $\varphi_{1,1}$ at the first plateau in time (see, e.g., figure 7, where the first plateau occurs at $t\omega_{A0} \approx 720$). From the simulations we can infer that $|\varphi_{sat\,1,1}| \propto (\gamma_L/|\omega_0|)^\alpha$, with $\alpha \approx 2$ for $\gamma_L/|\omega_0| \lesssim 0.15$, and $\alpha \lesssim 1$ for $\gamma_L/|\omega_0| > 0.15$. These results compare favorably, for weak drive, with the findings of [52], whereas, for sufficiently strong drive, are in fair agreement with that given in [31] and already anticipated in section 3 ($|\delta\boldsymbol{\xi}_r/r_s| \sim |\gamma_L/\omega_0|$), noting that $|\delta\boldsymbol{\xi}_r||\omega_0| \sim \mathbf{v}_{\delta\mathbf{E}\times\mathbf{B},r} \sim |\varphi_{1,1}|/r_s$.

4.3. Energetic electrons with density profile peaked off-axis

In this section the first global hybrid MHD-Gyrokinetic simulations of electron fishbones driven by energetic particles with density profile peaked off-axis [53] will be presented. This kind of equilibria is closely related to the experimental configuration in which electron fishbones have been observed in current devices. In these experiments, HFS off-axis heating is applied close to the q_{min} flux surface in the equatorial plane, using ECRH; thus, an inverted (positive) gradient of the energetic electron density profile is generated in the radial region of the discharge which is internal to the q_{min} flux surface and in which the internal kink can develop. Moreover, because of the HFS deposition, a selective heating on barely trapped/circulating particles will be obtained [6]. Recalling the stability condition, $\omega_{*Ee}/\omega > 0$ [5], and noting that ω_{*Ee} depends on the sign of the radial gradient of the energetic electron pressure profile, instability can occur only by resonance with energetic electrons characterized by precession reversal; i.e., barely trapped/circulating energetic particles [17, 18].

The equilibrium considered here has the same bulk density and temperature profiles and plasma parameters of the peaked on-axis one (see section 4.2 and figure 14 right), except for the inverse aspect ratio, $\epsilon = 0.1$, and the
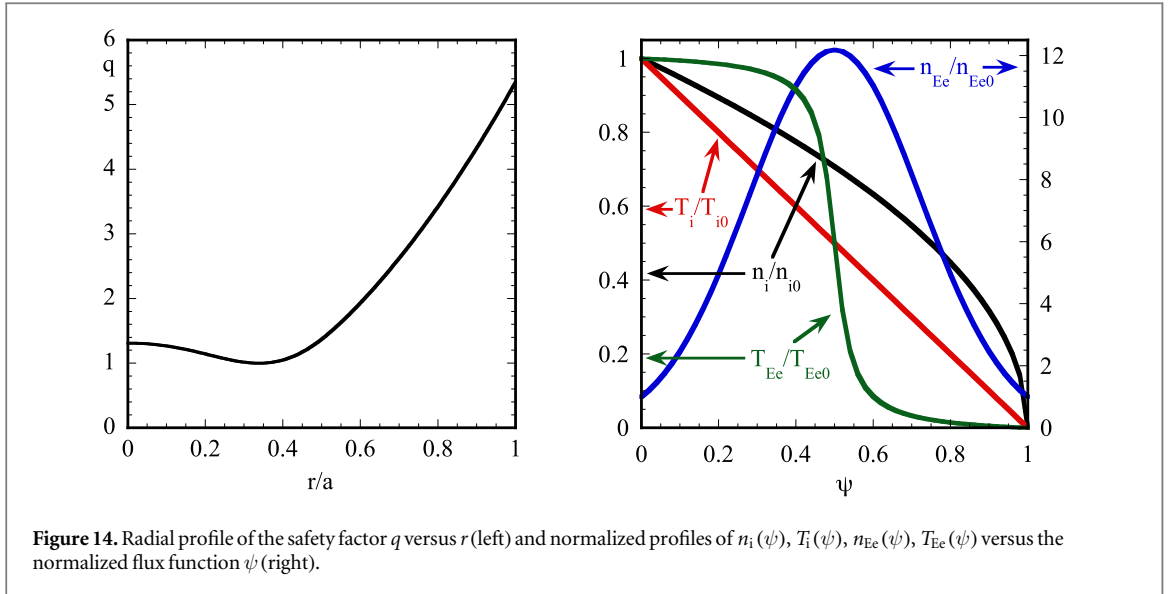
Figure 14. Radial profile of the safety factor q versus r (left) and normalized profiles of $n_i(\psi)$, $T_i(\psi)$, $n_{Ee}(\psi)$, $T_{Ee}(\psi)$ versus the normalized flux function ψ (right).
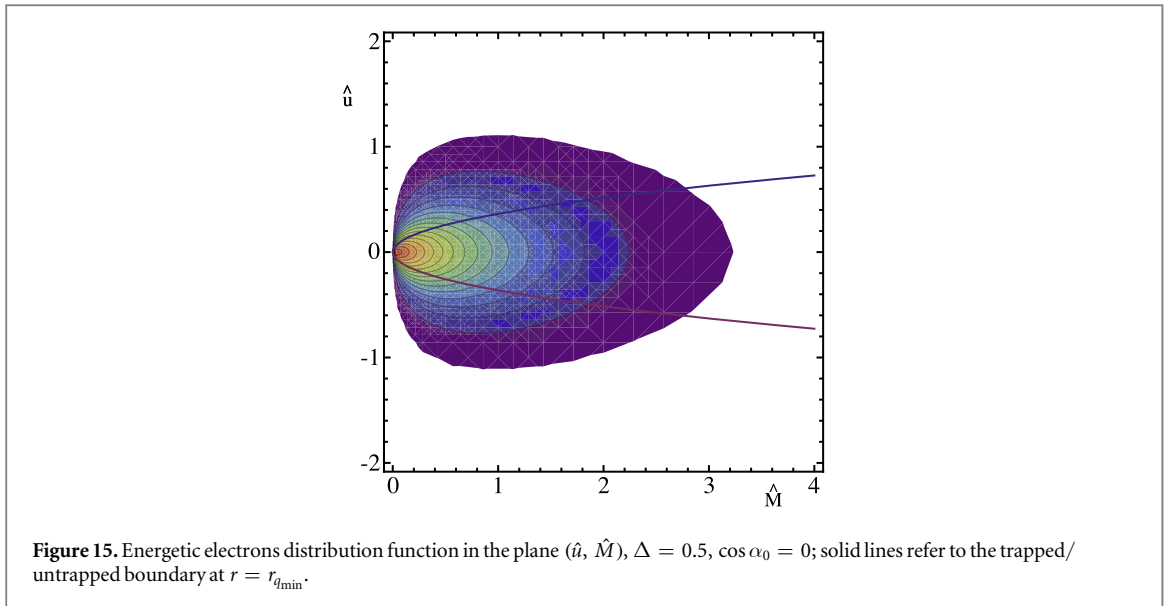

Figure 15. Energetic electrons distribution function in the plane $(\hat{u}, \hat{M})$, $\Delta = 0.5$, $\cos\alpha_0 = 0$; solid lines refer to the trapped/untrapped boundary at $r = r_{q_{min}}$.

safety factor profile q, which also in this case is slightly reversed with $q_0 \approx 1.3$, but with a q_{min} much closer to unity ($\Delta q \equiv 1 - q_{min} = 0.0002$) at the surface $r_{q_{min}}/a \approx 0.33$ and $q_a \approx 5.3$ (see figure 14 left). Note that $q_{min} \approx 1$ has been used in order to minimize the continuum damping and facilitate the occurrence of the energetic electron driven fishbone [7, 35]. Moreover, safety factor profiles with a reversed shear is known to enhance the reversal of precessional drift [17, 18, 54].
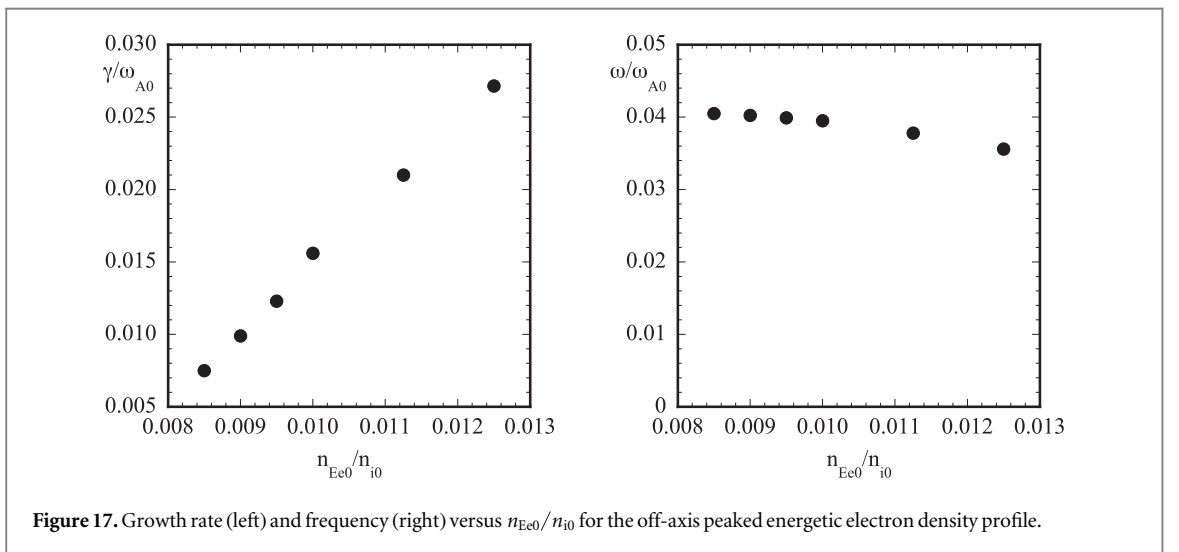
The energetic electrons radial density profile, peaked off-axis, has been chosen as $n_{Ee}(\psi)/n_{Ee0} = 12.1825 e^{-10(\psi-0.5)^2}$, with temperature radial profile

$$\frac{T_{Ee}(\psi)}{T_{Ee0}} = \frac{\arctan(-30\psi + 15) - \arctan(-15)}{2\arctan(15)},$$

and $T_{Ee0} = 50$ keV (see figure 14 right). The width Δ of the energetic electrons distribution function in the velocity space is $\Delta = 0.5$, whereas $\cos\alpha_0 = 0$ as for the energetic electron density profile peaked on-axis, see equation (7), and thus the distribution function is still symmetric in velocity space, and no net current is driven by energetic particles. The choice of $\Delta = 0.5$ is such to ensure the presence in the energetic electrons distribution function of a sufficient fraction of barely trapped/circulating particles (see figure 15). In the following simulations the toroidal mode number is $n = 1$, and the poloidal Fourier components retained are $m = 1, \ldots, 6$, normalized resistivity $S^{-1} = 3 \times 10^5$ and viscosity $\nu\tau_{A0}/a^2 = 3 \times 10^{-8}$, as before. Besides the kinetic contribution of the energetic electrons $(\nabla \cdot \mathbf{P}_{Ee})_\perp$, both the diamagnetic bulk ion term, and the thermal ion compressibility $(\nabla \cdot \mathbf{P}_i)_\perp$ treated kinetically are retained, whereas the contribution $(\nabla \cdot \mathbf{P}_e)_\perp$ of the bulk electrons will be neglected for simplicity, see equation (8). Moreover, the choice of a shaped energetic electron
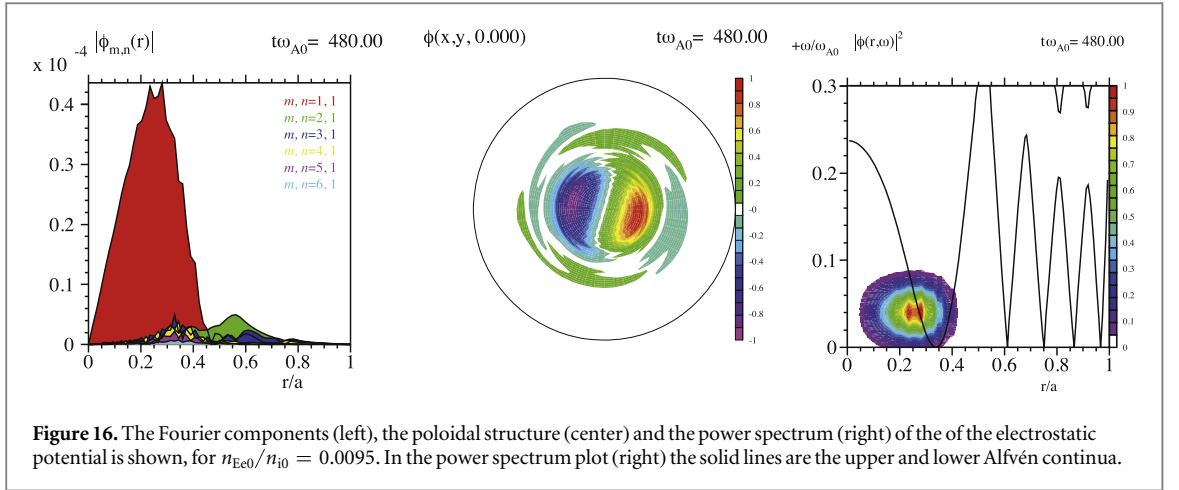
Figure 16. The Fourier components (left), the poloidal structure (center) and the power spectrum (right) of the of the electrostatic potential is shown, for $n_{Ee0}/n_{i0} = 0.0095$. In the power spectrum plot (right) the solid lines are the upper and lower Alfvén continua.
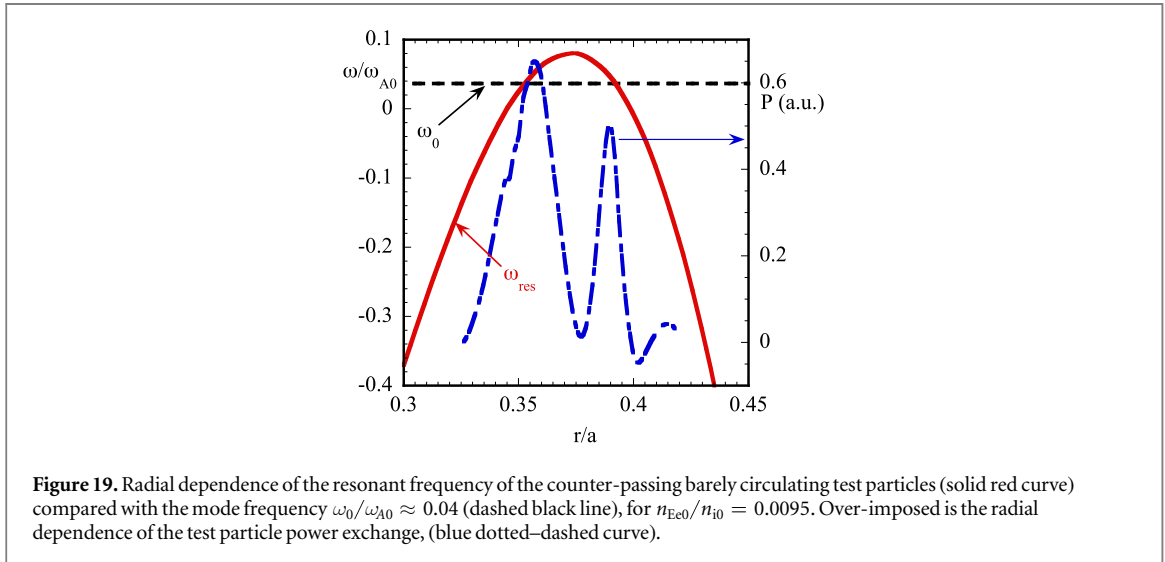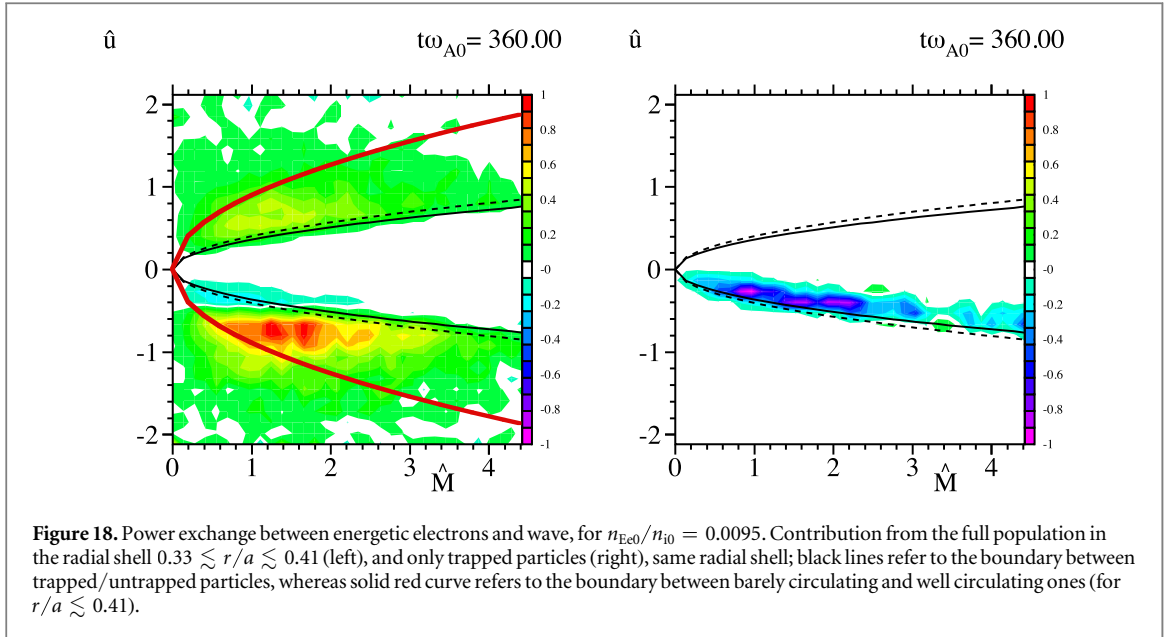

Figure 17. Growth rate (left) and frequency (right) versus n_{Ee0}/n_{i0} for the off-axis peaked energetic electron density profile.

temperature profile, which strongly decreases outside the $q \approx 1$ surface, has the beneficial effect of inhibiting the growth of modes with dominant poloidal mode numbers higher than unity, which can be driven unstable by deeply trapped energetic electrons outside the $q = 1$ surface, where the energetic electron density gradient becomes negative.

4.3.1. Linear dynamics

In this section we present linear dynamics results for the electron fishbone driven by energetic electron with off-axis peaked density profile. In figure 16 the radial profiles of the Fourier components, the poloidal structure and the power spectrum of the electrostatic potential are shown, for $n_{Ee0}/n_{i0} = 0.0095$: the radial structure of the poloidal Fourier components is dominated by the $m, n = 1,1$ component, which is localized in the region $q \lesssim q_{min}$, showing the characteristic shape of the internal kink radial displacement ($\xi_r \propto \varphi/r$). The structure of the mode in the poloidal plane rotates in time in the clock wise direction, i.e., opposite to the direction observed in the peaked on-axis EP radial profile (see section 4.2), which corresponds to a mode propagating in the direction of the diamagnetic velocity of the energetic electrons (which is parallel, for a peaked off-axis energetic electrons density profile, to the direction of the bulk ion diamagnetic velocity). The frequency of the mode is quite low, see figure 16 (right), as expected for equilibria with low values of Δq (see, e.g., [35]). In figure 17 the growth rate and frequency of the electron fishbone driven by energetic electrons with radial density profile peaked off-axis is shown: a linear dependence on n_{Ee0} is observed, above the threshold $n_{Ee0}/n_{i0} \approx 0.007$, with a real frequency weakly dependent on n_{Ee0}.

From the power exchange between the energetic electrons and wave, as shown in figure 18, it is possible to infer which fraction of energetic particles is driving the mode. In figure 18 (left) the power exchange in the radial shell $0.33 \lesssim r/a \lesssim 0.41$ is shown, with the curves approximating the trapped/untrapped boundary (solid black) and the barely/well circulating boundary (solid red) superimposed. Here, we follow the definition given in [7] for the barely circulating particles, defined as $(r/R)^{1/2} \lesssim \kappa^2 \lesssim 1$, with:
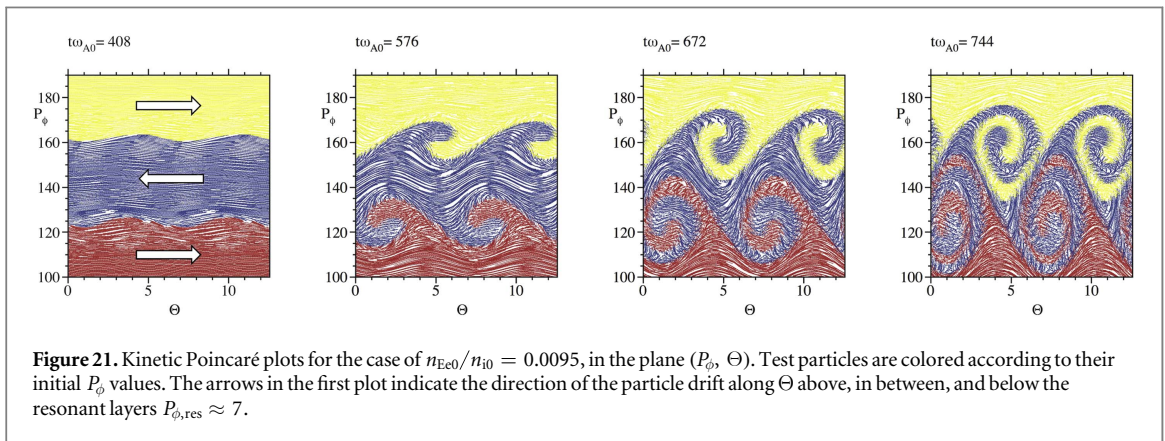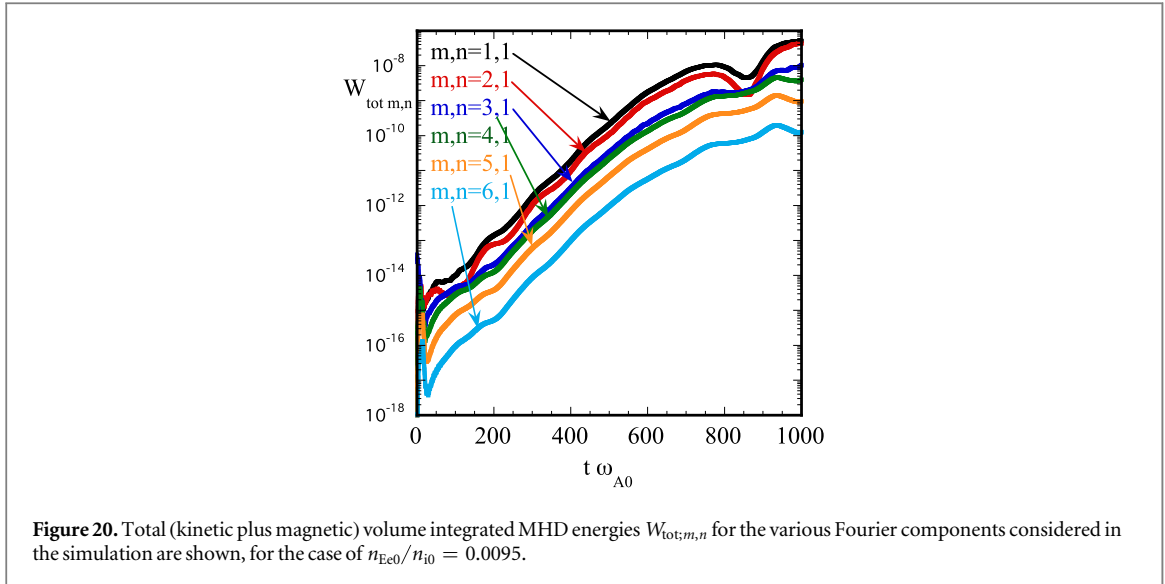
Figure 18. Power exchange between energetic electrons and wave, for $n_{Ee0}/n_{i0} = 0.0095$. Contribution from the full population in the radial shell $0.33 \lesssim r/a \lesssim 0.41$ (left), and only trapped particles (right), same radial shell; black lines refer to the boundary between trapped/untrapped particles, whereas solid red curve refers to the boundary between barely circulating and well circulating ones (for $r/a \lesssim 0.41$).

Figure 19. Radial dependence of the resonant frequency of the counter-passing barely circulating test particles (solid red curve) compared with the mode frequency $\omega_0/\omega_{A0} \approx 0.04$ (dashed black line), for $n_{Ee0}/n_{i0} = 0.0095$. Over-imposed is the radial dependence of the test particle power exchange, (blue dotted–dashed curve).

$$\kappa^2 = \frac{2(r/R_0)\lambda}{1 - (1 - r/R_0)\lambda}, \quad \lambda = \frac{\mu B_0}{\mathcal{E}}, \quad \mathcal{E} = \frac{v^2}{2}. \tag{9}$$

Indeed, the maximum power exchange occurs for particles in the region of velocity space belonging to that of barely circulating ones (in particular the counter-circulating ones, red pattern), with some minor contributions coming from the well circulating particles, both co- and counter-circulating (outside the solid red curve, green pattern); trapped particles, on the contrary, give a damping contribution (light blue to dark blue patterns) to the mode, as expected (see figure 18 (right), where only the power exchange due to trapped particles ($\kappa^2 > 1$) is shown in order to enhance the relative size of their contribution).

An analysis, similar to the one shown for the peaked on-axis energetic electrons density profile case, has been done for this simulation, in order to identify the characteristic resonance responsible for driving the mode. In particular, the Hamiltonian mapping technique has been applied to a set of test particles defined by the C_0, M_0 values corresponding to the region where the power exchange between energetic electrons and the wave is maximum in linear phase. This happens, for this simulation, for counter-passing barely circulating energetic particles at $r/a \approx 0.36$, $\hat{u} \approx -0.73$, $\hat{M} \approx 1.55$ (see figure 18 left), with a frequency of the mode $\omega/\omega_{A0} \approx 0.04$. In figure 19 the radial dependence of the resonant frequency of the circulating test particles $\omega_{res} = n\bar{\omega}_d + [\ell + (n\bar{q} - m)\sigma]\omega_b$, with $\ell = 0, m, n = 1, 1$ and $\sigma = -1$ (counter-passing particles) is compared with the observed frequency of the mode ω_0; also the radial profile of the power exchange between the test particles and the wave is presented, showing how the maximum power exchange correspond closely to the radii where the test particles are in resonance with the wave. In this case, the resonant condition is satisfied at two

Figure 20. Total (kinetic plus magnetic) volume integrated MHD energies $W_{\mathrm{tot};m,n}$ for the various Fourier components considered in the simulation are shown, for the case of $n_{\mathrm{Ee0}}/n_{\mathrm{i0}} = 0.0095$.

Figure 21. Kinetic Poincaré plots for the case of $n_{\mathrm{Ee0}}/n_{\mathrm{i0}} = 0.0095$, in the plane ($P_\phi$, Θ). Test particles are colored according to their initial P_ϕ values. The arrows in the first plot indicate the direction of the particle drift along Θ above, in between, and below the resonant layers $P_{\phi,\mathrm{res}} \approx 7$.

radial locations ('double resonance'), as a consequence of the $(q - 1)$ term in the resonant condition for circulating particles. Note that the variation of $\omega_{\mathrm{res}}(r)$ around the resonant positions is stronger than the one observed in the peaked on-axis EP density profile (being, for the two cases considered, $|\partial\omega_{\mathrm{res,off\text{-}axis}}/\partial r|/|\partial\omega_{\mathrm{res,on\text{-}axis}}/\partial r| \approx 4$); the effects of this difference will be manifest during the nonlinear saturation phase w.r.t. the peaked on-axis case.

4.3.2. Nonlinear dynamics

The evolution of the simulation with $n_{\mathrm{Ee0}}/n_{\mathrm{i0}} = 0.0095$ is shown in figure 20, where the time evolution of the total (kinetic plus magnetic) volume integrated MHD energies, $W_{\mathrm{tot};m,n}$, for the m, n Fourier components considered in the simulation are shown.

In figure 21 kinetic Poincaré plots are shown, for the test particles belonging to the subset (C_0, M_0) as described in the previous section, with the test particles colored according to their initial P_ϕ value: red color for the particles with $\hat{P}_\phi < \hat{P}_{\phi,\mathrm{res1}} \approx 125$ (corresponding to $r/a \lesssim r_{\mathrm{res1}}/a \approx 0.35$), blue color for particles with $\hat{P}_{\phi,\mathrm{res1}} \lesssim \hat{P}_\phi \lesssim \hat{P}_{\phi,\mathrm{res2}} \approx 162$ (i.e., $r_{\mathrm{res1}}/a \lesssim r/a \lesssim r_{\mathrm{res2}}/a \approx 0.39$), and yellow color for particles with $\hat{P}_\phi > \hat{P}_{\phi,\mathrm{res2}}$ (i.e., $r/a \gtrsim r_{\mathrm{res2}}/a$). Note that the double resonance structure, which has the sign of $\partial\omega_{\mathrm{res}}/\partial r$ at one resonant radius the opposite of that at the other resonant radius, makes particles in resonance at the inner radius rotating in the opposite direction w.r.t. the ones in resonance at the outer radius (see figure 21, second frame from left). While entering the fully nonlinear phase ($t\omega_{\mathrm{A0}} \gtrsim 670$, see figure 21, third frame from left), we note that the two island structures tend to insinuate oneself into the other, having a P_ϕ extension (or, equivalently, a radial extension) of the order of the distance between the two resonance layers $|P_{\phi,\mathrm{res2}} - P_{\phi,\mathrm{res1}}|$. As the test particles are displaced outside the resonant layer (toward $r < r_{\mathrm{res1}}$, or $r > r_{\mathrm{res2}}$), where the characteristic resonant frequency changes rapidly with radius (see figure 19), even changing its sign and, thus, not satisfying any more the instability condition $\omega_{*\mathrm{Ee}}/\omega > 0$, the mode has no 'convenience' in adjusting its frequency to that of the linearly resonant particles. Indeed, little variation of the frequency during the saturation phase is observed,
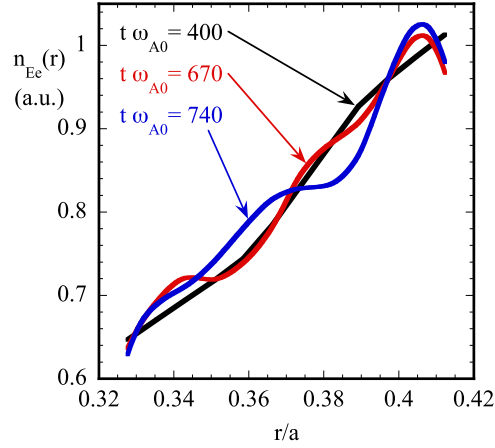
Figure 22. Density profile from test particles evolution: solid black curve corresponds to linear phase profile ($t\omega_{A0} = 400$), red and blue curves to nonlinear saturation phase profiles ($t\omega_{A0} = 670$ and $t\omega_{A0} = 740$).
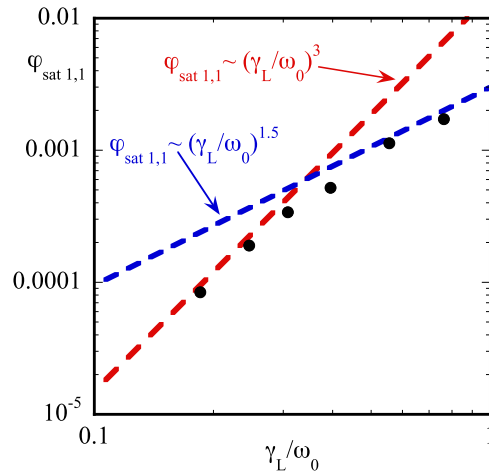
Figure 23. Saturation amplitude of $\varphi_{sat1,1}$ versus γ_L/ω_0 for the peaked off-axis energetic electron density profile.

and the saturation of this simulation can be ascribed to 'resonance detuning' (see, e.g., [14, 31, 34, 55]). The result of saturation on the radial density profile of the energetic particles is shown in figure 22: a flattening of the profile in a region somewhat larger than the one between the two resonant surfaces $r_{res1}/a \approx 0.35$ and $r_{res2}/a \approx 0.39$ is observed, the width of the flattened region being, nevertheless, quite small w.r.t. the $r_{q_{min}}$ region. Note that the radial density profiles, as obtained by the test particles, flatten around the two resonant radii at different times (in the case shown, at $t\omega_{A0} \approx 670$ for $r_{res1}/a \approx 0.35$, and $t\omega_{A0} \approx 740$ for $r_{res1}/a \approx 0.39$, see also the Poincaré plots, figure 21, third and fourth frame from left).

In figure 23 the scaling of the saturation amplitude of the electrostatic potential versus the ratio of the linear growth rate to the frequency of the mode γ_L/ω_0 is shown, in a scan in which the EP density is varied: a stronger scaling, $\varphi_{sat1,1} \approx (\gamma_L/\omega_0)^3$ is observed for values of $\gamma_L/\omega_0 \lesssim 0.3$, whereas for larger γ_L/ω_0 the scaling approaches $\varphi_{sat1,1} \approx (\gamma_L/\omega_0)^{3/2}$. These simulation results compare favorably with the analytic findings given at the end of section 3, where the scaling for the saturated displacement $|\delta\boldsymbol{\xi}_{r0}| \sim \gamma_L^3 |\omega_0|^{-3/2} |\Delta\omega|^{-3/2} |2\omega_0/\omega''_{res0}|^{1/2}$ was introduced, when noting that, in the case of $|\Delta\omega| > \gamma_L$ (corresponding to the low γ/ω values in figure 23) that scaling gives $|\varphi_{1,1\,sat}| \propto |\delta\boldsymbol{\xi}_{r0}||\omega_0|r_s \sim \gamma_L^3$, whereas for $|\Delta\omega| \sim \gamma_L$ one gets $|\varphi_{1,1\,sat}| \propto |\delta\boldsymbol{\xi}_{r0}||\omega_0|r_s \sim \gamma_L^{3/2}$.

5. Conclusions

In present days, e-fishbones have been observed on a variety of devices: they are internal kink-type instabilities driven by energetic electrons generated by, e.g., EC and/or LHH/current drive. A brief summary of experimental evidences have been given in section 2. Similarly to the well known ion fishbones, e-fishbones are

driven by wave-particle interaction at magnetic toroidal precession frequency of energetic electrons: they are characterized by linear dispersion relation similar to that of ion-fishbones (see section 3 for a brief summary of the theory of linear and nonlinear dynamics of e-fishbones). The large interest raised about the e-fishbones is also related to the fact that the radial transport, induced by fluctuations driven by magnetically trapped resonant particles, due to precession resonance, depends on energy and not mass of the particles themselves. Also, the energetic electrons on present devices are characterized by having much smaller resonant particle orbit width w. r.t. the characteristic scale length of the fishbone instability (which is of the order of the rigid radial displacement of the internal kink-like eigenfunction) similarly to what is expected for energetic ions (e.g., fusion α-particles) in burning plasmas, because of large plasma current, and differently from what can be obtained for energetic ions in present experiments. Thus, e-fishbones offer the opportunity to study both experimentally and numerically linear and nonlinear dynamics of wave-particles interactions relevant for fusion plasmas also on present, not ignited devices, and to compare with theory.

In the present paper, linear and nonlinear numerical simulations of fishbones driven by energetic electrons have been presented, using the hybrid MHD-Gyrokinetic code XHMGC [9]. Equilibria with both on-axis [8] and off-axis [53] peaked energetic electron radial density profile have been considered. For the on-axis peaked energetic electron radial density profile case, it has been enlightened the effects of considering the kinetic thermal ion compressibility and diamagnetic effects (in order to allow for an entirely novel treatment of enhanced inertia response and ion Landau damping) and the kinetic thermal electrons compressibility effects. The most important effect comes from the thermal ion compressibility treated kinetically, resulting in a considerable enhancing of the instability threshold energetic electron density. Resonances between wave and energetic electrons and thermal species have been analyzed using TPHM techniques [13, 14], clearly identifying the precession frequency $\bar{\omega}_d$ of deeply trapped energetic electrons in driving the mode [8]. Nonlinearly, the mode experiences a strong downward frequency chirping, adjusting its frequency in order to remain tuned with the resonant particles which are displaced outwardly; this results in keeping $|\dot{\Theta}| \approx 0$, the phase-locking condition, and induces the simultaneous flattening of the radial density profile of the resonant energetic particles together with the outward displacement of the resonance radial location. The process ends when the flattening of the resonant particles density profile approaches the q_{min} radius, where the internal kink eigenfunction, that remains almost unchanged in its shape during nonlinear phase, sharply decreases in amplitude ('radial decoupling', see [14]). Note that some of these features (chirping frequency, ejection of resonant particles) are consistent with previous findings of ion fishbone simulations [56]. The nonlinear saturation of the dominant Fourier component ($m/n = 1/1$) of the electrostatic potential, $\varphi_{sat1,1}$, has been shown to scale almost proportional to the strength of the ratio of the linear growth rate to the mode frequency, $\varphi_{sat1,1} \propto \gamma_L/\omega_0$, for sufficiently strong drive ($\gamma_L/\omega_0 \gtrsim 0.15$, for this particular simulation case), whereas stronger dependence is obtained in the weaker drive regime. The scaling obtained for strong drive, when the finite interaction length of the phase space zonal structures is of the order of the q_{min} radius, r_s, is consistent with the analytical findings [31], as reported in section 3.

In this paper we have also presented the first global hybrid MHD-Gyrokinetic simulations of electron fishbones driven by energetic particles with density profile peaked off-axis. Equilibria with off-axis peaked energetic electrons radial density profile are more closely related to the experimental conditions in which e-fishbones have been observed in current devices, where HFS off-axis heating using, e.g., ECRH forms barely trapped and/or barely circulating energetic electrons. These particles, because of the the toroidal precession reversal of their motion, can fulfill the instability condition $\omega_{*Ee}/\omega > 0$; the mode is observed to rotate poloidally in the direction of the diamagnetic velocity of the energetic electrons (which is parallel, for a peaked off-axis energetic electrons density profile, to the direction of the bulk ion diamagnetic velocity). In this equilibrium the radial structure of the resonance for the energetic electrons driving the mode is dominated by the $(q - 1)$ term entering in the expression of the resonance of circulating particles, see equation (3), thus having a double resonance in the vicinity of the q_{min} radial location r_s. Nonlinearly, kinetic Poincaré plots show a double island structure, one rotating in the opposite direction of the other, and shifted by π along the wave-particle phase Θ. Local flattening of the radial density profile of the resonant particles is observed in the radial positions of the double resonance, and no major frequency chirping is observed during saturation, which can be attributed to resonance detuning [14, 55]. The scaling of the saturated amplitude, for this equilibrium, is in good agreement with the predictions given in section 3: $\varphi_{sat1,1} \approx (\gamma_L/\omega_0)^3$ for weak drive, and $\varphi_{sat1,1} \approx (\gamma_L/\omega_0)^{3/2}$ when $|\Delta\omega| \equiv \omega_{res0} - \omega_0 \sim \gamma_L$.

It is worth noting that in this paper we have neglected the role of MHD nonlinearities, which are known to increase their importance near marginal stability [16, 36]. Thus, a more complete simulation study will be required to explore in detail the nonlinear dynamics also in these regimes of weak energetic electron drive.

Acknowledgments

References

[1] Aymar R, Chuyanov V, Huguet M, Parker R and Shimamura Y (The ITER Joint Central Team) 1997 *Proc. 16th Int. Conf. on Fusion Energy 1996* vol 1 (Vienna: International Atomic Energy Agency) p 3

[2] ITER Physics Basis *et al* *Nucl. Fusion* **39** 2137

[3] Fasoli A *et al* 2007 Progress in the ITER physics basis ch 5: physics of energetic ions *Nucl. Fusion* **47** S264

[4] McGuire K *et al* 1983 *Phys. Rev. Lett.* **50** 891

[5] Chen L, White R B and Rosenbluth M N 1984 *Phys. Rev. Lett.* **52** 1122–5

[6] Wong M *et al* 2000 *Phys. Rev. Lett.* **85** 996

[7] Zonca F *et al* 2007 *Nucl. Fusion* **47** 1588

[8] Vlad G, Briguglio S, Fogaccia G, Zonca F, Fusco V and Wang X 2013 *Nucl. Fusion* **53** 083008

[9] Wang X, Briguglio S, Chen L, Di Troia C, Fogaccia G, Vlad G and Zonca F 2011 *Phys. Plasmas* **18** 052504

[10] Zonca F, Chen L and Santoro R 1996 *Plasma Phys. Control. Fusion* **38** 2011

[11] Graves J P, Hastie R J and Hopcraft K I 2000 *Plasma Phys. Control. Fusion* **42** 1049

[12] Zonca F, Chen L, Botrugno A, Buratti P, Cardinali A, Cesario R and Pericoli Ridolfini V (JET-EFDA Contributions) 2009 *Nucl. Fusion* **49** 085009

[13] White R B 2012 *Commun. Nonlinear Sci. Numer. Simulat* **17** 2200–14

[14] Briguglio S, Wang X, Zonca F, Vlad G, Fogaccia G, Di Troia C and Fusco V 2014 *Phys. Plasmas* **21** 112301

[15] Heidbrink W W and Sadler G J 1994 *Nucl. Fusion* **34** 535

[16] Breizmann B N and Sharapov S E 2011 *Plasma Phys. Control. Fusion* **53** 054001

[17] Kadomtsev B B and Pogutse O P 1967 *Sov. Phys.—JETP* **24** 1172

[18] Kadomtsev B B and Pogutse O P 1971 *Nucl. Fusion* **11** 67

[19] Valovic M, Lloyd B, McClements K G, Warrick C D, Fielding S J, Morris A W, Pinfold T and Wilson H R (COMPASS-D Team and ECRH Team) 2000 *Nucl. Fusion* **40** 569

[20] Ding X *et al* 2002 *Nucl. Fusion* **42** 491

[21] Smeulders P, Buratti P, De Benedetti M and Monari G (FTU-team) 2002 *Proc. 29th EPS Conf. on Plasma Physics Controlled Fusion* vol 26B *(Montreux, Switzerland, 2002)* (ECA) D-5.016 (http://epsppd.epfl.ch/Montreux/start.htm)

[22] Romanelli F *et al* 2003 *Proc. 19th Int. Conf. on Fusion Energy* 2002 *(Lyon, France, 2002)* (Vienna: IAEA) (C&SPapersSeriesNo19/C) CD-ROM file Ov/4-5 (www.iaea.org/programmes/ripc/physics/fec2002/html/fec2002.htm)

[23] Maget P, Imbeaux F, Giruzzi G, Udintsev V S, Huysmans G T A, Ségui J-L, Goniche M, Moreau Ph, Sabot R and Garbet X 2006 *Nucl. Fusion* **46** 797

[24] Macor A *et al* 2009 *Phys. Rev. Lett.* **102** 155005

[25] Chen W *et al* 2009 *Nucl. Fusion* **49** 075022

[26] Chen W *et al* 2010 *Nucl. Fusion* **50** 084008

[27] Ding X T *et al* 2013 *Nucl. Fusion* **53** 043015

[28] Yu L M *et al* 2013 *Nucl. Fusion* **53** 053002

[29] Hongda H, Dong J Q, Zhao K, Zhixiong He, Chen W and Jiang H B 2014 *Nucl. Fusion* **54** 114001

[30] Chen W, Xu Y, Ding X T, Shi Z B, Jiang M, Zhong W L and Ji X Q H2-LA team 2016 *Nucl. Fusion* **56** 044001

[31] Chen L and Zonca F 2016 *Rev. Mod. Phys.* **88** 015008

[32] Zonca F and Chen L 2014 *Phys. Plasmas* **21** 072120

[33] Zonca F and Chen L 2014 *Phys. Plasmas* **21** 072121

[34] Zonca F, Chen L, Briguglio S, Fogaccia G, Vlad G and Wang X 2015 *New J. Phys.* **17** 013052

[35] Merle A, Decker J, Garbet X, Sabot R, Guimarães-Filho Z and Nicolas T 2012 *Phys. Plasmas* **19** 072504

[36] Ödblom A, Breizman B N, Sharapov S E, Hender T C and Pastukhov V P 2002 *Phys. Plasmas* **9** 155

[37] White R B, Goldstone R J, McGuire K, Boozer A H, Monticello D A and Park W 1983 *Phys. Fluids* **26** 2958

[38] Idouakass M, Faganello M, Berk H L, Garbet X and Benkadda S 2015 *42nd EPS Conf. on Plasma Physics* vol 39E *(Lisbon Portugal, 22–26 June 2015)* paper P2.165 (http://ocs.ciemat.es/EPS2015PAP/html/contrib.html)

[39] Vlad G, Kar C, Zonca F and Romanelli F 1995 *Phys. Plasmas* **2** 418–41

[40] Briguglio S, Vlad G, Zonca F and Kar C 1995 *Phys. Plasmas* **2** 3711–23

[41] Briguglio S, Zonca F and Vlad G 1998 *Phys. Plasmas* **5** 3287–301

[42] Park W *et al* 1992 *Phys. Fluids* B **4** 2033

[43] Izzo R, Monticello D A, Park W, Manickam J, Strauss H R, Grimm R and McGuire K 1983 *Phys. Fluids* **26** 2240

[44] Briguglio S, Vlad G, Zonca F and Fogaccia G 2002 *Phys. Lett.* A **302** 308–12

[45] Zonca F, Briguglio S, Chen L, Dettrick S, Fogaccia G, Testa D and Vlad G 2002 *Phys. Plasmas* **9** 4939–56

[46] Briguglio S, Fogaccia G, Vlad G, Zonca F, Shinohara K, Ishikawa M and Takechi M 2007 *Phys. Plasmas* **14** 055904

[47] Vlad G, Briguglio S, Fogaccia G, Zonca F, Di Troia C, Heidbrink W W, Van Zeeland M A, Bierwage A and Wang X 2009 *Nucl. Fusion* **49** 075024

[48] Vlad G, Briguglio S, Fogaccia G and Zonca F 2004 *Plasma Phys. Control. Fusion* **46** S81–93

[49] Vlad G, Briguglio S, Fogaccia G, Zonca F and Schneider M 2006 *Nucl. Fusion* **46** 1–6

[50] Cardinali A *et al* 2010 *Fusion Energy 2010* (Vienna: IAEA) THW/P7-04 (www-naweb.iaea.org/napc/physics/FEC/FEC2010/html/fec10.htm)

[51] Di Troia C, Briguglio S, Fogaccia G, Vlad G and Zonca F 2012 *24th IAEA FEC 2012 (San Diego, 8–13 October 2012)* TH/P6-21(www-naweb.iaea.org/napc/physics/FEC/FEC2012/html/proceedings.pdf)

[52] O'Neil T M, Winfrey J H and Malmberg J H 1971 *Phys. Fluids* **14** 1204

[53] Fusco V, Vlad G, Briguglio S and Fogaccia G 2015 *14th IAEA Technical Meeting on Energetic Particles in Magnetic Confinement Systems (Wien, Vienna, Austria, 1–4 September 2015)* (International Atomic Energy Agency) p 28

[54] Kessel C, Manickam J, Rewolt G and Tang W M 1994 *Phys. Rev. Lett.* **72** 1212

[55] Wang X, Briguglio S, Lauber Ph, Fusco V and Zonca F 2016 *Phys. Plasmas* **23** 012514

[56] Fu G Y, Park W, Strauss H R, Breslau J, Chen J, Jardin S and Sugiyama L E 2006 *Phys. Plasmas* **13** 052517

[57] Ponti G *et al* 2014 *Proc. 2014 Int. Conf. on High Performance Computing and Simulation, HPCS 2014* pp 1030–3 art. no. 6903807